



ELSEVIER

Physica D 151 (2001) 271–304

PHYSICA D

www.elsevier.com/locate/physd

Meta-stability of equilibrium statistical structures for prototype geophysical flows with damping and driving

Mark T. DiBattista^a, Andrew J. Majda^{a,*}, Marcus J. Grote^b

^a *Courant Institute of Mathematical Sciences, New York University, 251 Mercer Street, New York, NY 10012, USA*

^b *Department of Mathematics, ETH Zürich, Switzerland*

Received 5 March 1999; received in revised form 5 December 2000; accepted 1 February 2001

Communicated by C.K.R.T. Jones

Abstract

The most-probable states of an equilibrium statistical theory, which consist of monopole vortices, dipole vortex streets, and zonal shear flows for various parameter regimes, are shown to be meta-stable with respect to damped and driven quasi-geostrophic dynamics in a periodic β -plane channel. Through a series of numerical experiments that include (1) pure decay, (2) both damping and driving, and (3) both direct and inverse cascades of energy, we demonstrate that statistically most-probable states evolve into other most-probable states with high accuracy, even as the energy changes substantially and the flow undergoes topological transitions from vortex to shear flow, or vice versa. The predictions of the equilibrium statistical theory are calculated by an algorithm, which we call an “approximate dynamics”, that constructs the most-probable states from the instantaneous values of a few quantities in the evolving flow. Qualitatively, the approximate dynamics predicts the correct topological structure — whether vortex flow or zonal shear — in the evolving flow. Quantitatively, the predictions are evaluated by measuring the relative errors between the velocity fields and vorticity fields of the evolving flow and the most-probable states. For evolving monopole vortices we find that errors in the velocity field are generally near 5% and errors in the potential vorticity field are generally near 15%. For evolving dipole vortex streets, the magnitude of the relative errors depends on the amplitude of the localized forcing. For pure decay, the errors in the velocity field are generally near 5% and errors in the vorticity field are generally near 12%; for runs in which the flow is strongly forced by small-scale vortices whose amplitude is nearly $\frac{3}{10}$ the peak vorticity in the initial flow, the errors in the velocity field can rise to 20% and the errors in the vorticity field rise to 40%. © 2001 Elsevier Science B.V. All rights reserved.

Keywords: Coherent structure; Equilibrium statistical theory; Meta-stability

1. Introduction

The prevalence and persistence of large-scale vortical structures amid the turbulent cascades of stratified geophysical flows — structures such as the Great Red Spot, or the vortex streets in the zonal jets and bands of Jupiter [14], the gulf stream rings, or blocking vortex dipole pairs in Earth’s mid-latitudes [6] — has long presented a challenge to atmospheric and oceanographic researchers. One attractive approach to this problem is

* Corresponding author. Tel.: +1-212-998-3324; fax: +1-212-995-4121.
E-mail address: jonjon@cims.nyu.edu (A.J. Majda).

through equilibrium statistical mechanics, which produces large-scale monopolar and dipolar vortex structures as the most-probable states at statistical equilibrium. In this paper, we test a recent equilibrium statistical theory, described in [21] and investigated in [4], via an approximate dynamics for a strongly damped and driven quasigeostrophic (QG) flow in a periodic channel on a β -plane, which is among the simplest barotropic models for geophysical phenomena at mid-latitudes. We demonstrate here that equilibrium solutions of the statistical theory are meta-stable, i.e., that these solutions, which are stable for inviscid dynamics, are practically unchanged for long times when dissipation and forcing are present. This is demonstrated by showing that statistically most-probable states tend to evolve into other most-probable states under damping and driving in QG dynamics, even as the fluid undergoes topological transitions from vortex flows to zonal shear flows, or vice versa.

Equilibrium statistical theories predict the state of a fluid at statistical equilibrium given only the value of essential invariants in the flow. The earliest equilibrium theory considered only two such invariant quantities, the energy and enstrophy [11]. The energy–enstrophy theory, which yields a linear relation between the mean-field stream and vorticity fields, has had some success in geophysical contexts, most notably in flows dominated by topography [2,10,19] and in flows with low energies and minimal enstrophy that satisfy the conditions of selective decay [1]. More recent theories, which are fully nonlinear, attempt to treat the entire infinite list of invariant quantities in ideal flow, which includes the energy and all possible rearrangements of the initial vorticity field [15,18]. However, the suitability of the infinite-constraint theories to geophysical flows, which are strongly damped and driven in time, is in question, since the higher-order moments of the vorticity field, which must be specified in these theories, have little influence upon the mean-field predictions and are never known exactly.

Indeed, recent theoretical and numerical work suggests that it is preferable to base the equilibrium theory on just a few judicious quantities [8,9,13]. Turkington [21] shows that these quantities depend on the distribution of vorticity: for flows in which the vorticity is predominantly either positive or negative the essential invariants include the energy, circulation, and vorticity extrema in the flow. For flows in which the vorticity is both positive and negative the essential invariants include the energy, circulation, and the “absolute vorticity”

$$A = \int |\bar{q}|, \quad (1.1)$$

where $q = \omega + \beta y$ is the potential vorticity in QG flow [16]. Here, ω is the usual vorticity and the geophysical parameter β incorporates the dynamic consequences of the Earth’s curvature into the channel model.

In [4] the equilibrium statistical theory based on these invariants is adapted for barotropic flow on a β -plane channel with eastward mean flow, V . The full set of prototype geophysical solutions is calculated for a wide range of parameter values. The most-probable states for flows with predominantly single-signed potential vorticity are zonal shears at low energies and vortex monopoles at high energies (see (3.11)). The most-probable states for flows with vorticity of both signs are zonal shears at low energies and dipole vortex streets at high energies (see (3.13)). The prototype solutions produced by the equilibrium theory also exhibit an intrinsic Rhines’ scale, where the emergence of vortices from the underlying shear flow is inhibited by increasing the β -parameter [17]. We have already successfully applied another version of the theory, modified for two-layer QG flow in a rectangular basin, as a simple model for the spreading phase of open-ocean convection [3,12].

In this paper, we apply the equilibrium statistical theory to *evolving* damped and driven geophysical flows. In Section 4, we describe an approximate dynamics that calculates the most-probable states of the equilibrium theory whose energy, circulation and other essential quantities match the instantaneous values of the evolving flow. Thus, by tracking the values of only a few key quantities, we approximate the state of the evolving flow

with the most-probable solutions of equilibrium statistical mechanics. Our purposes in this paper are therefore twofold:

- To demonstrate the meta-stability of the most-probable states of equilibrium statistical theory, i.e., vortex monopoles and vortex dipole streets, under a wide range of numerical experiments involving small-scale forcing and dissipation. This study includes both direct and inverse cascade regimes — flow regimes in which energy transfers from large to small scales where dissipation is more efficient and flow regimes in which strong small-scale forcing near the scales of resolution allows substantial energy transfer to the largest scales. However, our resolution is too crude to compute detailed spectra for these cascades and these are not the quantities of primary interest here. We establish here the suitability of the solutions of the statistical theory as basic models of atmospheric and oceanographic structures.
- To evaluate quantitatively the accuracy of the equilibrium statistical theory — how well do the predictions of the Langevin and dilute-vortex theory track the evolution of large-scale coherent structures in a strongly damped and driven flow? In this respect this paper serves as a validation study of the approximate dynamics.

These goals are realized through a series of numerical runs initialized by monopole vortices and dipole vortex streets that are the most-probable states produced by the equilibrium theory. The numerical experiments include cases of pure decay in Section 5, in which only the dissipation is active, and cases with both dissipation and forcing in Section 6, in which small-scale vortices — mimicking the bombardment of the flow by localized storms — are randomly placed in the channel domain. Additionally, in a more stringent test of the theory, we compare the endstate that arises from an inverse cascade — induced by single-signed, small-scale forcing of an initially quiescent channel — to the most-probable states of the equilibrium theory.

How well does this simple procedure perform? We introduce two measures that quantify the accuracy of the approximate dynamics: we calculate the relative error in the velocity and vorticity fields, defined in (2.12) and (2.13), between snapshots in the evolving flow and the equilibrium predictions of the approximate dynamics. In general, we expect the errors in the vorticity field to be greater than errors in the velocity field, due to the small dimples in the vorticity field caused by the small-scale forcing not yet sheared by the large-scale flow. In Table 1, we summarize the quantitative results for a numerical runs undergoing both dissipation and small-scale forcing.

Here, Amp is a measure of the strength of the small-scale forcing, which is defined in (2.9). In addition to the low relative errors, the approximate dynamics procedure accurately predicts the topological structure — whether vortex flow or zonal shear — of the evolving flow. We show many examples in which the procedure tracks the topological transitions in the numerical experiments, usually pinpointing the times in which the vortices cross over to shear flows, or vice versa.

Finally, this paper is organized as follows: we introduce the QG fluid model and all issues related to the numerical experiments in Section 2; a very brief discussion to the equilibrium statistical mechanics and the maximum-entropy structures produced by the theory is provided in Section 3; a detailed description of the approximate dynamics is given in Section 4; the numerical experiments subject to free decay are analyzed in Section 5; the numerical

Table 1

Solution class	Amp	Velocity error (%)	Vorticity error (%)
Monopole	Free decay	5	15
Monopole	0.1 peak PV	5	15
Dipole street	Free decay	5	12
Dipole street	0.1 peak PV	10	20
Dipole street	0.3 peak PV	20	40

experiments subject to both damping and driving are analyzed in Section 6; and a concluding section summarizing the results of the paper appears in Section 7.

2. Numerical model

2.1. Quasigeostrophic fluid model

In this paper, we consider one of the simplest models for geophysical flow at mid-latitudes, the barotropic QG fluid in a β -plane channel. Specifically, we consider a QG fluid that is both damped and driven in a unit β -plane channel periodic in x with the extent $-\frac{1}{2} < x < \frac{1}{2}$ and $-\frac{1}{2} < y < \frac{1}{2}$. For nonvanishing mean flow, V , the stream function, $\Psi = -Vy + \psi$, and the potential vorticity, $q = \Delta\Psi + \beta y$ satisfy

$$\frac{\partial q}{\partial t} + \nabla^\perp \Psi \cdot \nabla q = \mathcal{D}(\Delta)\omega + \mathcal{F}, \quad \omega = \Delta\Psi, \quad (2.1)$$

where \mathcal{D} represents the dissipation

$$\mathcal{D}(\Delta) \equiv \sum_{i=0}^3 d_i (-1)^i \Delta^i, \quad d_i \geq 0, \quad (2.2)$$

and \mathcal{F} represents the small-scale forcing by localized vortices of radius r ,

$$\mathcal{F}(x, y, t) = \sum_{j=1}^{\infty} \delta(t - j\Delta t) \omega_r(\vec{x} - \vec{x}_j), \quad (2.3)$$

which is described more fully in Section 2.3. For the dissipation operator, \mathcal{D} , in (2.2), the coefficient d_0 represents the Ekman drag, which models the effect of the boundary layer on large-scale geophysical flows, d_1 represents Newtonian viscosity, which models molecular diffusion, and d_3 represents hyperviscosity, which ensures numerical stability in flows with vanishing Newtonian viscosity. The hyperviscosity coefficient d_2 vanishes for all numerical experiments treated in this paper.

The boundary conditions for QG dynamics in (2.1) satisfy the condition of no normal flow at the channel edges and are periodic in x , so that we have

$$\frac{\partial \psi}{\partial x} = 0, \quad y = \pm \frac{1}{2}, \quad \psi\left(-\frac{1}{2}, y, t\right) = \psi\left(\frac{1}{2}, y, t\right). \quad (2.4)$$

Here, the corresponding fluid velocity is given by

$$\vec{v} = \nabla^\perp \Psi = \begin{pmatrix} V \\ 0 \end{pmatrix} + \begin{pmatrix} -\frac{\partial \psi}{\partial y} \\ \frac{\partial \psi}{\partial x} \end{pmatrix}, \quad (2.5)$$

and ψ is normalized so that

$$\psi(x, \frac{1}{2}, t) = \psi(x, -\frac{1}{2}, t). \quad (2.6)$$

The requirement in (2.6) guarantees that

$$\int_{-1/2}^{1/2} \int_{-1/2}^{1/2} \vec{v}(x, y) \, dx \, dy = \begin{pmatrix} V \\ 0 \end{pmatrix}, \quad (2.7)$$

so that V is the mean flow velocity along the x -axis. Here and below, \vec{x} denotes $\vec{x} = (x, y)$. For more detail on the QG model, see [16].

2.2. Numerical method

We solve the QG equations in (2.1) numerically using a pseudospectral method, which calculates the gradients $\nabla^\perp \psi$ and $\nabla \omega$ in Fourier space, and the nonlinear product $\nabla^\perp \psi \cdot \nabla \omega$ at the mesh points in physical space. The resolution of the numerical grid varies from 64×64 to 256×256 for the numerical experiments treated in this paper, see Fig. 12 for a comparison at two different resolutions. The particular implementation, used by Grote and Majda [8], advances the solution in time by an explicit second-order split-step method, whose main advantage over an explicit Runge–Kutta method is the exact treatment of the diffusive terms — here, there is no stability constraint on the size of the time step due to the stiff diffusive terms. The time-stepping is adaptive to ensure stability as the flow speed accelerates. In order to de-alias the high frequencies, which appear due to spatial and temporal truncation errors, we use an exponential filter developed earlier by E and Shu [5].

2.3. Random forcing

The forcing in the QG fluid in (2.1) is designated by the variable \mathcal{F} , which represents a bombardment of the flow by small-scale storms in the vorticity field. These small vortices, which have finite support and constant amplitude, are placed at random mesh points in the flow at fixed time intervals, and take the particular form

$$\mathcal{F}(x, y, t) = \sum_{j=1}^{\infty} \delta(t - j \Delta t) \omega_r(\vec{x} - \vec{x}_j), \quad (2.8)$$

where the j th vortex is centered at \vec{x}_j . Each of these localized vortices has support in a small disk of radius r_j , given by

$$\omega_r(\vec{x}) = \begin{cases} \text{Amp} \left(1 - \frac{|\vec{x} - \vec{x}_j|^2}{r_j^2} \right)^2, & |\vec{x} - \vec{x}_j|^2 \leq r_j^2, \\ 0, & |\vec{x} - \vec{x}_j|^2 > r_j^2. \end{cases} \quad (2.9)$$

Here, the parameter Amp represents the strength of the vortex and may be either positive or negative, corresponding to cyclonic or anticyclonic forcing.

The term \mathcal{F} in (2.8) is determined by four parameters: the vortex strength, Amp, the vortex radius, r_j , the vortex position, \vec{x}_j , and the time interval, Δt . In each of the experiments described in this paper the random locations \vec{x}_j are uniformly distributed among the mesh points inside the unit channel domain, excluding a narrow margin along the channel boundaries. The radius r_j of the small-scale vortices is fixed at $\frac{3}{64}$. The time interval between forcings is fixed at $\Delta t = 0.1$, which in all cases is at least 10 times larger than the time step used for the numerical integration of the (nonlinear) advection terms — if the simulation is run up to $T = 1000$, precisely 10,000 small-scale vortices are added to the evolving flow, while at least 100,000 time steps are performed by the numerical method. The main parameter that varies from experiment to experiment is therefore the vortex strength, Amp, which is usually expressed as a proportion of the maximum initial potential vorticity in the flow.

2.4. Quantitative measures

In this paper, the quantitative comparisons between the evolving flow and the most-probable states of the equilibrium theory are evaluated by means of the correlation between two functions, i.e.,

$$\text{Corr}(f, g) = 1 - \frac{(f, g)^2}{\|f\|^2 \|g\|^2}, \quad (2.10)$$

in which (f, g) denotes the L_2 -inner product on the channel domain and $\|f\|$ its corresponding L_2 -norm. The correlation satisfies $0 \leq \text{Corr}(f, g) \leq 1$ and the correlation is zero if and only if the functions f and g are collinear, i.e.,

$$f = \mu g, \quad (2.11)$$

where μ is any nonzero constant.

In addition, we have two different error measures that quantify the accuracy of the equilibrium theory in reproducing the evolving flow: the relative L_2 -error in the velocity

$$\text{Err}(\vec{v}, \vec{v}^*) = \frac{\|\vec{v} - \vec{v}^*\|_2}{\|\vec{v}\|_2}, \quad (2.12)$$

and the relative L_2 -error in the vorticity

$$\text{Err}(\omega, \omega^*) = \frac{\|\omega - \omega^*\|_2}{\|\omega\|_2}, \quad (2.13)$$

in which the unstarred quantities represent snapshots in the evolving flow and starred quantities refer to the maximum-entropy state. In general, we expect that the relative error in the vorticity is a more severe test than the corresponding error in the velocity, since the velocity field is usually “smoother” than the vorticity field.

2.5. Selective-decay theorem

In decaying flow the ratio of enstrophy to energy, Λ ,

$$\Lambda = \frac{\int (q - \beta y)^2}{|\vec{v}|^2}, \quad (2.14)$$

where $q - \beta y$ is the *relative* vorticity and \vec{v} the velocity in the flow, is of particular interest due to the selective-decay theorem [7,13]. This theorem predicts that the vorticity of decaying solutions to the Navier–Stokes equations in doubly periodic geometry asymptotically approaches a ground state, which is given by the eigenfunction associated with the smallest eigenvalue of the Laplacian operator, Δ , for the periodic domain. Moreover, the enstrophy–energy ratio, Λ , in (2.14), asymptotically approaches the smallest eigenvalue of the Laplacian from above as the flow decays.

The proofs of Foias and Saut can be adapted for the contexts of this paper [20] — where the dissipative mechanism is Ekman drag with hyperviscosity, the flow frequently has uniformly positive circulation, and the flow domain is a periodic channel — and in decaying numerical runs we typically see a uniform decrease in the enstrophy–energy ratio, Λ , towards the value determined by the ground state, which is the smallest eigenfunction of the Laplacian consistent with the symmetries imposed by the periodic channel and the initial distribution of vorticity. Indeed, for decaying monopole vortices comprised of single-signed vorticity in a unit channel, we have

$$\Lambda(t) \rightarrow \pi^2, \quad (2.15)$$

which is the eigenvalue associated with the ground state potential vorticity field given by $q = \sin(\pi y)$. For decaying dipolar vortex pairs with vanishing circulation in a unit channel, we have

$$\Lambda(t) \rightarrow 4\pi^2, \quad (2.16)$$

which is the eigenvalue associated with the ground state potential vorticity field given by $q = \sin(2\pi y)$.

It is well established that the simplest equilibrium statistical theories accurately predict the asymptotic ground state solutions for purely decaying flow as the coarse-grained limiting fluctuations [11,13]. Indeed, the ground state potential vorticity and streamfunction satisfy the linear mean-field equation produced by the energy–enstrophy theory. Our goal in this paper is to track evolving flow fields in which vortices dominate, as the result of both direct and inverse cascades in numerical runs with both damping and driving. In these vortex regimes the ground state solutions, which consist entirely of zonal shear flows in a periodic channel, cannot possibly track the evolving flow accurately. In Section 3, we develop the simplest nonlinear equilibrium theories that are useful for the QG dynamics in (2.1)—these nonlinear theories produce vortex flows as the most-probable states at sufficiently high energies. Furthermore, the trend in the enstrophy–energy ratio in (2.14) provides a simple test that determines whether a flow is approaching a ground state—and thus a zonal shear—or has sufficient energy in the small scales to support a vortex in the large-scale flow.

3. Summary of equilibrium statistical theory

In an evolving two-dimensional ideal fluid, undulations in the smallest scales of the potential vorticity typically increase, which is a consequence of the so-called direct cascade of enstrophy. However, even as these undulations dominate the finest scales, well-organized coherent structures are observed to emerge at the largest scales in the potential vorticity field. As the fluid approaches a state of statistical equilibrium the variations in the small-scale vorticity field therefore appear as fluctuations about a large-scale mean-field state, within which most of the energy in the flow resides.

The goal of equilibrium statistical mechanics is to predict the large-scale coherent structures that emerge in a fluid at statistical equilibrium, given only the initial values of essential invariant quantities in the flow. For a QG flow satisfying (2.1) with vanishing dissipation, $\mathcal{D} = 0$, and forcing, $\mathcal{F} = 0$, the total list of invariant quantities is infinite, and includes the energy, E

$$E = \int (q(\vec{x}) - \beta y)\psi(\vec{x}), \quad (3.1)$$

and all functions of the initial vorticity field

$$\int \mathcal{G}(q), \quad (3.2)$$

where \mathcal{G} is an arbitrary function.

The most-probable state at statistical equilibrium is expressed as the solution to a *mean-field equation* that relates the mean-field values of the potential vorticity, \bar{q} , and streamfunction, $\bar{\psi}$ that emerge at statistical equilibrium via

$$\bar{q} = f(\bar{\psi}; E_0, \dots), \quad \bar{q} = \bar{\psi} + \beta y. \quad (3.3)$$

The solutions to the mean-field equation in (3.3) are constrained by the initial values of the energy, $E = E_0$, in (3.1) and some set, either finite or infinite, of the vortical invariants listed in (3.2). Furthermore, the form of the mean-field equation in (3.3) ensures that

$$\nabla \bar{q} \cdot \nabla^\perp \bar{\psi} = 0, \quad (3.4)$$

so that the most-probable states of the equilibrium theory are steady. By and large, the various equilibrium statistical theories are distinguished by the number and form of the conserved quantities in (3.2) that constrain the mean-field solution of (3.3).

However, the invariant quantities listed in (3.2) are not all equally important; in particular, the higher-order moments of the vorticity field may vary without any noticeable effect upon the largest scales of the mean-field potential vorticity. Since we wish to apply the equilibrium theory to evolving flows that are strongly dissipated and repeatedly forced by small-scale vortices — which is characteristic of the atmosphere and oceans — it is preferable to construct a theory based on only a few judicious quantities from the infinite list in (3.2) [8,9,13].

Of the infinite list of conserved quantities in (3.2) which are essential? Turkington [21] argues that two broad classes of flow must be distinguished: (1) those in which the potential vorticity is predominantly either positive or negative, and (2) those in which the potential vorticity is distributed among both signs. In each of these two cases we choose different invariants from the infinite list in (3.2) that lead to different forms of the mean-field equations in (3.3). We treat each of these cases separately in the following two sections.

3.1. Equilibrium statistical theory for channel flow with predominantly single-signed PV (Langevin theory)

For flows in which the potential vorticity is predominantly either positive or negative the following quantities from the infinite list in (3.1) and (3.2) are essential:

<i>Quantity</i>	<i>Definition</i>	<i>Lagrange multiplier</i>	
Energy	$E = \int (q - \beta y)(\psi)$	θ	(3.5)
Circulation	$\Gamma = \int (q - \beta y)$	γ	
PV extrema	$Q_+ = \max(q), Q_- = \min(q)$	None	

It can be shown [4] that for the given initial values of energy, $E = E_0$, circulation, $\Gamma = \Gamma_0$, and potential vorticity extrema, Q_+ and Q_- , the mean-field equation in (3.3) for QG flow in a β -plane channel takes the particular form

$$\bar{q} = \Delta \bar{\psi} + \beta y = \bar{Q} + Q \mathcal{L}[Q(\theta \bar{\psi} - \gamma)], \quad (3.6)$$

which along with the boundary conditions in (2.4), yields the mean-field streamfunction, $\bar{\psi}$, and potential vorticity field, \bar{q} , predicted as the most-probable state by the equilibrium theory. Here, we have $\mathcal{L}(x) \equiv \coth(x) - 1/x$, which is known as the Langevin function, and the parameters \bar{Q} and Q in (3.6) are related to the vorticity extrema Q_+ and Q_- in (3.5) via

$$\bar{Q} = \frac{1}{2} Q_+ + Q_-, \quad Q = \frac{1}{2} Q_+ - Q_-. \quad (3.7)$$

Since the mean-field equation has the form of a Langevin function, the equilibrium theory based on the conserved quantities in (3.5) is known as the Langevin equilibrium theory.

The Langevin mean-field equation in (3.6) contains the Lagrange multipliers, θ and γ , which are associated with the energy constraint and circulation constraints, respectively (see the right-hand column of (3.5)). The Lagrange multipliers are evaluated to ensure that the energy, E , and circulation, Γ , of the most-probable state take on the specified values, E_0 and Γ_0 , respectively. There are no Lagrange multipliers for the constraints on the potential vorticity extrema, since these parameters enter directly into the mean-field equations in (3.6). The mean-field equation in (3.6) is solved and the Lagrange multipliers θ and γ are evaluated by an iterative numerical method described in [22].

3.2. Equilibrium statistical theory for channel flow with PV of both signs (dilute-vortex theory)

For flows comprised of both positive and negative potential vorticity the following quantities from the infinite list in (3.1) and (3.2) are essential:

<i>Quantity</i>	<i>Definition</i>	<i>Lagrange multiplier</i>	
Energy	$E = \int (q - \beta y)(\psi)$	θ	(3.8)
Circulation	$\Gamma = \int (q - \beta y)$	γ	
Absolute vorticity	$A = \int \bar{q} $	α	

It can be shown [4] that for the given values of energy, $E = E_0$, circulation, $\Gamma = \Gamma_0$, and absolute vorticity, $A = A_0$, the mean-field equation in (3.3) for QG flow in a β -plane channel takes the particular form

$$\bar{q} = \Delta \bar{\psi} + \beta y = \frac{2(\theta(\bar{\psi} - Vy) - \gamma)}{\alpha^2 - (\theta(\bar{\psi} - Vy) - \gamma)^2}. \quad (3.9)$$

Here, θ , γ , and α are the Lagrange multipliers, listed in the right-hand column of (3.8), associated with the energy, circulation, and absolute vorticity constraints, respectively. The numerical evaluation of these variables in the mean-field equations in (3.3) ensures that the energy, E , circulation, Γ , and absolute vorticity, A , of the most-probable state take on the specified values, E_0 , Γ_0 , and A_0 , respectively.

Notice that there is no constraint on the vorticity maxima in the smallest scales in (3.8). Formally, the equilibrium theory based on the conserved quantities listed in (3.8) arises in the limit as (a) the magnitude of the peak vorticity in the smallest scales diverges and (b) this peak vorticity is very dilutely mixed in a surrounding bath of neutral vorticity. The equilibrium theory that gives rise to the mean-field equation in (3.8) is therefore known as the dilute-vortex theory [21].

A more detailed derivation of the mean-field equations in the Langevin theory in (3.6) and dilute-vortex theory in (3.9) is found in [4]. A complete description of the algorithm that numerically solves the mean-field equations and determines the value of the Lagrange multipliers is found in [22].

3.3. Structure of the most-probable states

Solutions to the mean-field equations for the Langevin theory in (3.6) and the dilute-vortex theory in (3.9) form the basis of the approximate dynamics that is central to this paper. In both theories the most-probable solutions are shear flows at low energies and vortex flows at high energies.

For vanishing mean flow, V , and β -parameter, the most-probable solutions in the Langevin theory, which solve the mean-field equation in (3.6), are symmetric with respect to the center of the channel, i.e.,

$$\bar{q}(x, y) = \bar{q}(x, -y). \quad (3.10)$$

The low energy shear flows appear as a central ridge (or trough) in the potential vorticity field that extends the length of the channel. At sufficiently high energies, monopole vortices emerge from the central ridge (or trough), see Fig. 3A and B for two examples. Thus, for flows with predominantly either positive or negative potential vorticity, the most-probable structures are

Most-probable solutions in Langevin theory :	Low energy	Shear flow	(3.11)
	High energy	Monopole vortex	

For vanishing mean flow, V , β -parameter, and circulation, Γ , the most-probable solutions in the dilute-vortex theory, which solve the mean-field equation in (3.9), exhibit a diagonal symmetry with respect to the channel center, i.e.,

$$\bar{q}(x, y) = -\bar{q}(-x, -y). \quad (3.12)$$

At low energies, the shear flow in the dilute-vortex limit is comprised of a ridge and trough in the potential vorticity field, arranged antisymmetrically across the channel center. At high energies a cyclonic vortex emerges from the

ridge and an anticyclonic vortex emerges from the trough, and are arranged in a staggered fashion to form a vortex street. Thus, for flows which contains large amounts of both positive and negative potential vorticity, we have

$$\text{Most-probable solutions in dilute-vortex theory :} \quad \begin{array}{ll} \text{Low energy} & \text{Shear flow} \\ \text{High energy} & \text{Dipole vortex streets} \end{array} \quad (3.13)$$

See Fig. 3C and D for two examples.

The activation of the remaining parameters — the eastward mean flow, V , the β -parameter, and the circulation, Γ — does not change the basic structure of the most-probable state of the equilibrium theory, i.e., the most-probable structures remain zonal shear flows, monopole vortices, and dipole vortex streets. However, these parameters do alter the form of the solutions in important ways. For the monopole structure, the sign of the vortex, whether cyclonic or anticyclonic, is determined by the sign of the circulation. The position of the monopole center — whether it lies in the upper or lower half of the channel — is determined by the nondimensional ratio of β to eastward mean flow, V .

For the dipole vortex streets, the impulse of the ensemble, whether positive (cyclonic vortex in the upper half of the channel, anticyclonic vortex in the lower half of the channel) or negative (vice versa), is determined by the nondimensional ratio of β to eastward mean flow, V . A positive (negative) circulation strengthens (weakens) the cyclonic vortex in the pair and weakens (strengthens) the anticyclonic vortex. For a more complete discussion of the role of the various parameters and their qualitative effects on solutions to the mean-field equations, see [4], especially Table 2 in that paper.

It is possible to derive other types of solutions to the mean-field equations than those listed in (3.11) and (3.13) by further restricting the symmetries of the candidate solutions considered in the equilibrium theory. These solutions are not the overall most-probable configurations of potential vorticity, but only among those configurations that belong to a given symmetry class. Thus it is possible to calculate shear flow solutions to the mean-field equations in (3.6) or (3.9) that have identical energy, circulation and other parameter values as the more-probable vortex solutions.

The equilibrium statistical theory also predicts a generalized Rhines' scale that governs the transition boundary between the most-probable coherent vortex structures and zonal shear flows [4,17]. These transition curves in the

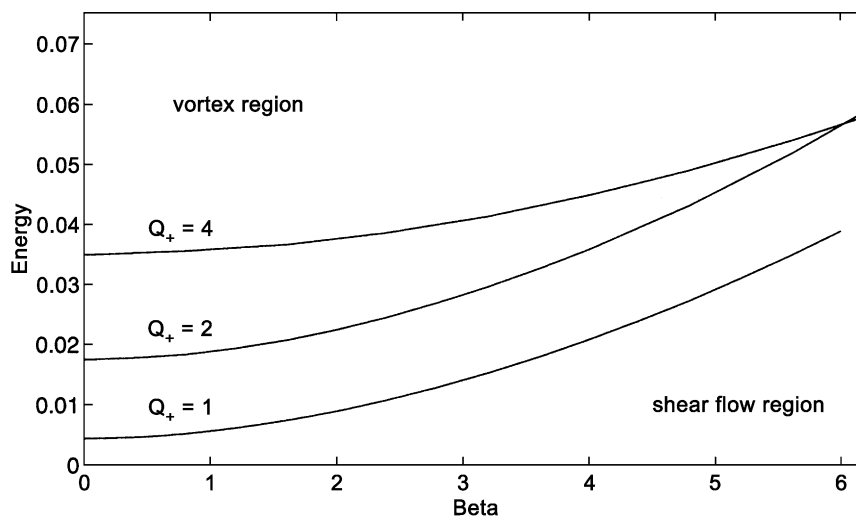


Fig. 1. Three curves in the β -energy plane that show that topological transitions of the most-probable state from zonal shear to vortex flow. For each of these three cases, which hold for vorticity maximum $Q_+ = 1, 2,$ and 4 , the vortex region lies above and to the left to the curve and the shear flow region lies below and to the right.

(E, β) -plane exactly follow parabolas for both monopole vortices and vortex streets. Thus these transitions yield consistent length scales for a wide range of β -parameters and energies. This implies that, for a given value of energy, the strength of vortices is weakened by an increasing β -parameter, and that there always exists a value of β above which the most-probable states are zonal shear flows. In Fig. 1, we provide a set of transition curves that demonstrate the Rhines' effect for solutions of the Langevin mean-field equations in (3.6) for three values of Q_+ (the vorticity minimum vanishes, $Q_- = 0$). Each curve is a parabola; however, the curvature decreases as the potential vorticity maximum, Q_+ , increases. Based on the shape of these parabolic curves, we anticipate that numerical experiments run at higher β -parameter are more likely to yield zonal shear flows.

4. Approximate dynamics for Langevin and dilute-vortex theory

4.1. Mean-field quantities

We check the accuracy and consistency of predictions from the equilibrium statistical theory for evolving damped and driven flow by an algorithm that we call the *approximate dynamics*. We extract key quantities from snapshots of the evolving flow, including the mean-field energy and circulation, produce the most-probable states in the equilibrium statistical theory based on this limited information, and calculate the accuracy of the fit based on the statistical measures on the velocity and vorticity fields given in (2.12) and (2.13).

Before we provide the algorithm for the approximate dynamics, we must deal with one subtlety of the equilibrium theory. The approximate dynamics must be based entirely on *mean-field* quantities, i.e., the mean-field potential vorticity, \bar{q} , or streamfunction, $\bar{\psi}$, since these are predicted by the equilibrium theory and observed in the evolving flow. The mean-field equations in (3.3) are derived from “coarse-graining” the information that appears in the smallest scales. Of all the infinite invariants of ideal flow listed in (3.1) and (3.2), it can be shown that only two are unchanged by the process of coarse-graining — the energy, E , and circulation, Γ [13,15]. Therefore, the energy, E , and circulation, Γ , may be written as functions of the mean field

$$E = \int (q - \beta y)(\psi) = \int (\bar{q} - \beta y)(\bar{\psi}), \quad (4.14)$$

$$\Gamma = \int (q - \beta y) = \int (\bar{q} - \beta y), \quad (4.15)$$

where the small-scale streamfunction, ψ , and vorticity field, q , are simple replaced by the coarse-grained, mean-field quantities, $\bar{\psi}$ and \bar{q} .

The remaining quantities, which are the vorticity extrema Q_+ and Q_- in the Langevin theory (see the bottom row of (3.5)) and the absolute vorticity, A , in the dilute-vortex theory (see the bottom row of (3.8)), must be estimated from the mean-field data. Indeed, one of the aims of this paper is to produce effective mean-field surrogates in the approximate dynamics for these small-scale quantities.

For the Langevin theory, this is quite simple. The potential vorticity maximum, Q_+ , in (3.5) in the flow is estimated from the maximum potential vorticity in the preexisting flow and the additional potential vorticity provided by the forcing, which yields

$$Q_+ = \max(\bar{q}) + \text{Amp} + \text{small amount}, \quad (4.16)$$

where Amp is the amplitude of the forcing discussed in Section 2.3 and the “small amount” is usually a few percent of maximum in the mean-field potential vorticity. The addition of a “small amount” tacitly acknowledges the possible insufficiency of estimating small-scale information from the large-scale field; however, as a practical matter we provide ample evidence that the best fit between the evolving flow and the equilibrium statistical theory is given by

\bar{q} and Amp alone. We may define a similar relation for the vorticity minima, Q_- , in (3.5), but in all the numerical experiments run with predominantly single-signed vorticity in Section 5, we assume the quantity vanishes, i.e. $Q_- = 0$, with no practical loss in accuracy of the equilibrium theory.

We cannot measure the absolute vorticity, A , defined in (1.1), in the evolving flow, since this quantity depends on the details of the small-scale potential vorticity field. Therefore, we must find a related mean-field quantity that we can measure from mean-field data and that is in one-to-one correspondence with A for all equilibrium solutions produced by the dilute-vortex theory. The simplest such quantity is the related “mean-field absolute vorticity”, \bar{A} :

$$\bar{A} = \int_D |\bar{q}| \, dx \, dy. \quad (4.17)$$

The quantity, \bar{A} , in (4.17) is unambiguously determined from the mean-field potential vorticity field. Furthermore, to show that there is a one-to-one correspondence between the absolute vorticity, A in (1.1), and the mean-field absolute vorticity, \bar{A} in (4.17)—so that we may freely replace one quantity with the other—we show a set of solution curves produced by the dilute-vortex equilibrium statistical theory plotted in the (E, \bar{A}) -plane in Fig. 2. Thus, at any point in the diagram there is a unique most-probable solution to dilute-vortex equilibrium theory, given an arbitrary energy and mean-field absolute vorticity. The α -parameter that appears in the figure is the Lagrange multiplier conjugate to the absolute vorticity and is evaluated to ensure that the most-probable solution possesses the appropriate energy and absolute vorticity. Should there be any indeterminacy in the procedure, the various solution curves in Fig. 2 would cross, a condition that does not occur.

4.2. Algorithm for the approximate dynamics

The equilibrium statistical theory for the damped and driven QG flow in (2.1) is evaluated quantitatively via an approximate dynamics based on the mean-field equations in (3.6) for the Langevin theory used in the numerical experiments described in Section 5, or in (3.9) for the dilute-vortex theory used in the numerical experiments described in Section 6. The form of the algorithm for the approximate dynamics is identical for both theories and may be summarized as follows:

1. For each numerical experiment, we specify the dissipation, \mathcal{D} , the forcing \mathcal{F} , and the initial vorticity field and evolve the flow by the QG dynamics in (2.1).
2. At fixed time intervals, we calculate the instantaneous values of energy, E , and circulation, Γ .
For the algorithm based on the Langevin theory we calculate the potential vorticity extrema, Q_+ , in (4.16).
For the algorithm based on the dilute vortex theory we calculate the mean-field absolute vorticity, \bar{A} in (4.17).
3. The values of the Lagrange multipliers θ , γ , and possibly α are determined to ensure that the energy, circulation, and possibly the mean-field absolute vorticity of the most-probable states match the values calculated from the evolving snapshots.
4. We calculate the correlation, and relative errors in the vorticity and velocity fields between the instantaneous snapshots and the predictions made by the equilibrium theory.

Thus, we have defined an unambiguous algorithm for the approximate dynamics for the Langevin and dilute-vortex equilibrium statistical theories described in Section 3. This algorithm is based entirely on mean-field quantities that are easily calculated from snapshots of the evolving flow.

5. Statistical consistency of freely decaying vortex states

We turn now to the numerical experiments that establish the meta-stability of monopole and dipole vortices through both direct and inverse cascades and the quantitative accuracy of the approximate dynamics described in

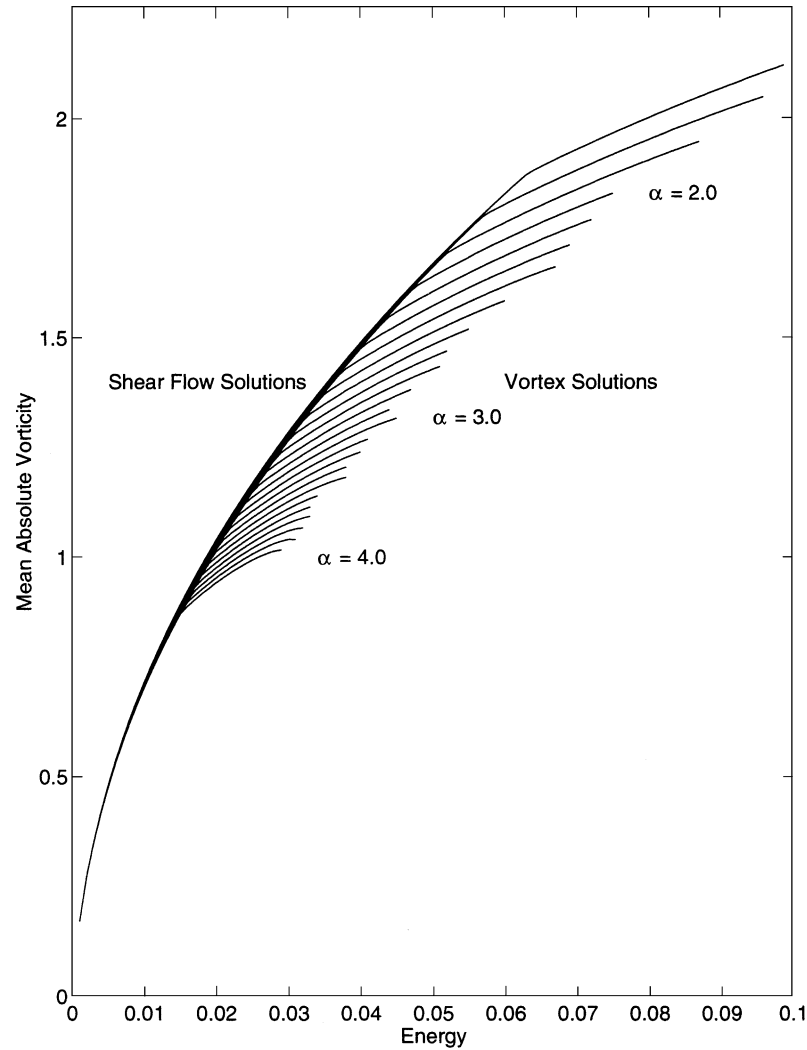


Fig. 2. Most-probable solutions in the dilute-vortex theory plotted in the energy-mean absolute vorticity plane. Shear flow solutions lie on the closely spaced curves on the left-most portion of the figure, vortex solutions lie on the separated curves on the right. None of the individual curves cross in the diagram.

Section 4. We concentrate on two kinds of experiments: (1) the free decay of vortical flows, which is treated in this section, and (2) the damping and driving of large-scale vortices by small-scale forcing, which will be discussed in Section 6.

The numerical experiments are initialized with monopole and dipole vortices produced as the most-probable states of the equilibrium statistical theories described in Section 3. Here, the initial vortices freely decay and we show that a fluid initialized with an equilibrium state will evolve “close” to other such equilibrium solutions, even as the energy substantially decays and the streamlines exhibit topological transitions as vortical flows decay into shear flows. We have shown in Fig. 1 that geophysical flows tend towards shear flows; the results of this section show that the equilibrium statistical theory is quite successful at tracking the topological transition from vortex to

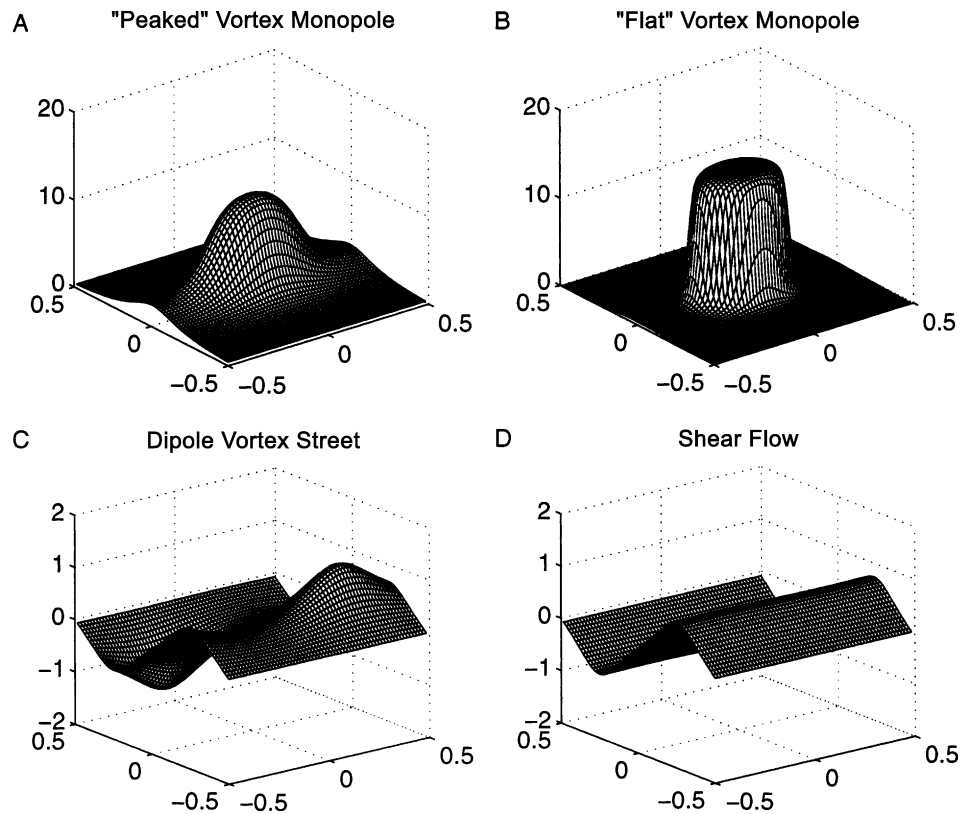


Fig. 3. Initial potential vorticity surfaces for the numerical experiments run in this paper. Each surface is the most-probable state produced by the statistical theory. (A) The “peaked” monopole vortex with energy, $E = 0.4$, circulation, $\Gamma = 2.225$ and $\beta = 0.5$. (B) The “flat” monopole vortex with energy, $E = 0.4$, circulation, $\Gamma = 1.85$, and $\beta = 0.5$. (C) A dipole vortex street with energy, $E = 0.0034$, mean absolute vorticity, $\bar{A} = 0.42$, and $\beta = 0.1$. (D) A shear flow with energy $E = 0.0034$, mean absolute vorticity, $\bar{A} = 0.42$, and $\beta = 0.1$.

shear flow. These simple laminar tests of the consistency of the statistical theory also provide a point of comparison for the numerical experiments run with small-scale forcings that are described in Section 6. Quantitative measures between the evolving flow and the most-probable states of the statistical theory are summarized in Table 1 and show that the approximate dynamics is quite successful in tracking the evolution of freely decaying runs, with relative errors near 5% in the velocity field, as defined in (2.12), and between 12 and 15% in the vorticity field as defined in (2.13).

5.1. Free decay of vortex monopoles

To illustrate the free decay of vortex monopoles, we initialize the flow with one of two different cases, shown in Fig. 3A and B. The monopole in Fig. 3A is “peaked”, and the potential vorticity is gently distributed throughout the channel. The monopole in B is “flat”, and the potential vorticity is sharply divided into two patch-like regions. These vortices, which are both most-probable states in the Langevin statistical theory, have identical energy, $E = 0.4$, but differing circulations—the circulation in the peaked example is $\Gamma = 2.225$, and the circulation in the flat example is $\Gamma = 1.85$. The turnaround time for both vortices is near $t = 3$; this is estimated by dividing the mean circumference of the vortex, $d = 2\pi r = \pi/2$, by the “average” velocity in the initial flow, which is estimated at

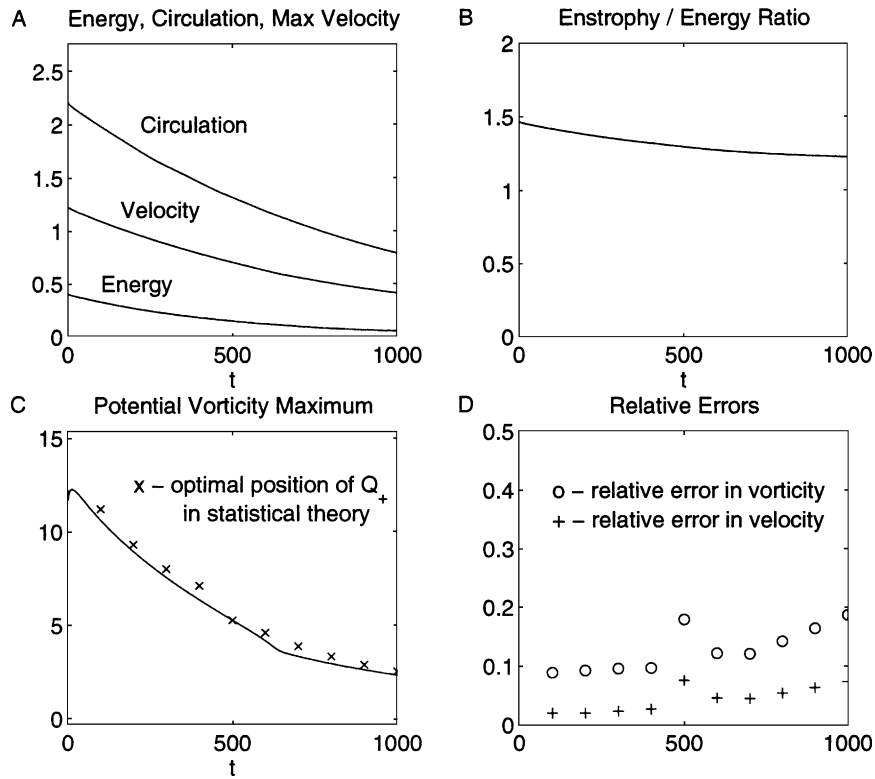


Fig. 4. Evolving quantities for free decay of peaked monopole shown in Fig. 3A, damped by a combination of Ekman drag, $d_0 = 10^3$, and hyperviscosity, $d_3 = 10^{-7}$. (A) The energy, circulation and maximum velocity in the flow. (B) The enstrophy–energy ratio normalized by π^2 . (C) The maximum potential vorticity in the flow and the optimal positions produced by the statistical theory. (D) The relative errors with respect to vorticity field, marked by \circ , and with respect to the velocity field, marked by \times .

approximately half the peak velocity, $v = 1.2/2$, so that we have

$$\text{Vortex turnaround time} = \frac{\pi}{2 \times 0.6} \sim 3. \quad (5.1)$$

For the experiments initialized with a peaked vortex and dissipated by Ekman drag and hyperviscosity, the total run time is usually $T = 1000$, so that the run lasts for more than 300 vortex turnaround times. For the experiments initialized with a flat vortex undergoing Newtonian viscosity, Reynolds number is near $Re \sim 2500$, and the total run time is $T = 50$.

In our first numerical experiment the peaked monopole, depicted in Fig. 3A, freely decays, dissipated by a combination of Ekman drag, $d_0 = 10^{-3}$, and hyperviscosity, $d_3 = 10^{-7}$. The geophysical β -parameter is $\beta = 0.5$. The total run time is $T = 1000$, which is sufficiently long for the initial vortex to decay into a shear flow, which occurs near time $t = 630$. The energy and circulation decrease uniformly throughout the run and the maximum of the potential vorticity increases for a short time after initialization due to the hyperviscosity, which is shown in Fig. 4A and C. Also, the maximum velocity, in the flow, v_{\max} ,

$$v_{\max} = \max|\vec{v}| \quad (5.2)$$

decreases in the evolution of the flow.

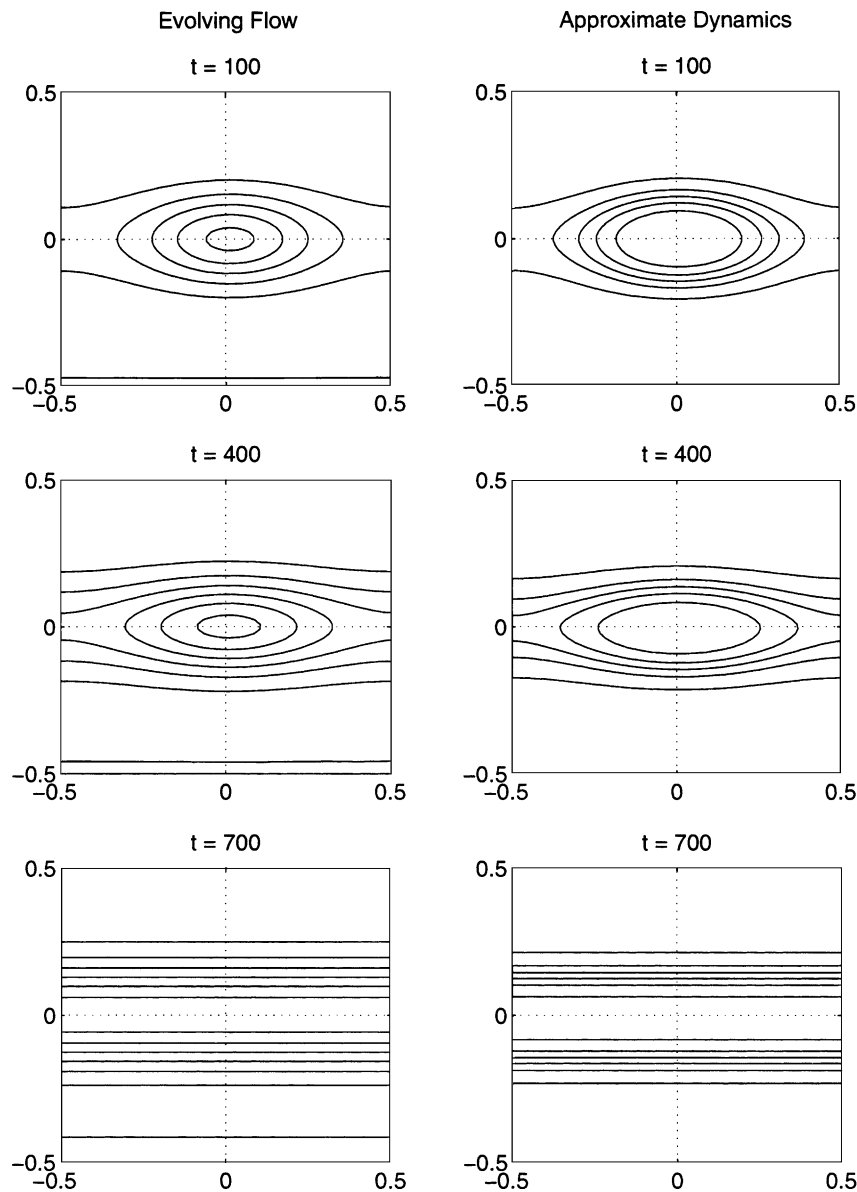


Fig. 5. Contour lines of the potential vorticity fields at times $t = 100, 400,$ and 700 for the numerical experiment described in Fig. 4. Left-hand column: snapshots of the evolving flow; right-hand column: most-probable states of the statistical theory.

Three snapshots of the decaying flow are shown in the left-hand column of Fig. 5 at times $t = 100, 400,$ and 700 , for the contour lines of the potential vorticity. The equilibrium solutions of the approximate dynamics, which are produced by the algorithm described in Section 4, appear at the corresponding positions in the right-hand column of Fig. 5. The equilibrium solutions are calculated from the instantaneous values of the evolving energy, circulation, and potential vorticity maximum that appear in Fig. 4. During the numerical experiment the initial vortex slowly weakens and decays to a zonal shear flow at time near $t = 630$ —therefore, two of the snapshots depict vortex

flows and one depicts a zonal shear. The qualitative structure of the decaying flow in the left-hand column of Fig. 5 is clearly captured by the approximate dynamics, which also pinpoints the time at which the evolving flow crosses from vortex to shear flow.

Each of the most-probable solutions in Fig. 5 is very near the *optimal*, in the sense of correlations defined in (2.10), that the approximate dynamics can produce. At each time we extract the instantaneous values of the energy and circulation, and solve the Langevin mean-field equations in (3.6) for a range of potential vorticity extrema, Q_+ , in (4.16). The values of the potential vorticity maximum that yields the smallest correlations for each snapshot are plotted with \times 's in Fig. 4C — notice that almost all lie just above the maximum PV in the mean field. This supports the use of (4.16) in the approximate dynamics.

The quantitative comparisons, as measured by the relative errors in the velocity and vorticity fields, see (2.12) and (2.13), between the evolving and approximate dynamics are shown in Fig. 4D. The errors are roughly constant in the early stages of the experiment for times $t < 500$, where the topological structure is a strong monopole. The relative errors in the velocity field are near 2% and relative errors in the vorticity field near 9%. As the monopole vortex weakens and approaches the crossover point to zonal shear flow, there is a bump in the quantitative data, after which the errors slowly increase throughout the run, with relative errors in the velocity field approximately 3–8% and relative errors in the vorticity field approximately 9–20%.

Finally, the evolution of the ratio of enstrophy to energy, Λ , defined in (2.14), shows that the freely decaying solution is approaching the ground state. The ratio is uniformly decaying to the limiting value of π^2 , as predicted by the selective-decay theorem described in Section 2.5.

We have also run freely decaying numerical experiments initialized with the flat monopole shown in Fig. 3B, examples of which are not shown. For runs in which the dissipation is the identical combination of Ekman drag, with $d_0 = 10^{-3}$, and hyperviscosity, $d_3 = 10^{-7}$, we see an interesting and subtle degradation of the approximate dynamics. In the early times of the numerical run, a large peak of potential vorticity forms in the center of the monopole, which is caused by the nonpreservation of vorticity maxima by hyperviscosity. Since this abrupt initial behavior violates one of the constraints upon which the Langevin statistical theory is based — the conservation of potential vorticity extrema, Q_+ and Q_- , in (3.5) — we might expect that the approximate dynamics performs less well for initially flat vortices than for initially peaked vortices. Although the initial vortex state is nearly patch-like, the hyperviscosity has created, by time $t = 100$, a build-up of potential vorticity in the center of the monopole — it increases from 14 to nearly 18 — and smoother gradients at the vortex edges. The approximate dynamics apparently cannot reappportion the vorticity in such a manner that follows the hyperviscosity and simultaneously dissipates the energy and circulation in a manner determined by the Ekman drag.

We might expect to improve matters by replacing the dissipation with straightforward Newtonian viscosity, $d_1 = 0.01$, with no additional hyperviscosity. For this case the qualitative behavior of the evolving vortex monopole remains unchanged, and the vortex decays into a shear flow. However, the predictions of the statistical theory for dissipation under Newtonian viscosity follow the decay of monopole vortices more closely than for pure decay under Ekman drag and hyperviscosity, since the statistical theory produces monopoles whose tops are flattened. These numerical experiments show the subtle effect of the quantities that are nearly preserved in the evolving flow and that form the basis of the equilibrium statistical theory.

5.2. Free decay of vortex streets

To illustrate the free decay of vortex streets, we initialize the flow by the most-probable state shown in Fig. 3C and evolve under the QG dynamics in (2.1) with $\mathcal{F} = 0$. The dissipation, \mathcal{D} , is a combination of Ekman drag, $d_0 = 10^{-3}$ and hyperviscosity, $d_3 = 10^{-7}$. The turnaround time for the vortices is near $t = 12$; this is estimated by dividing the mean circumference of a vortex, $d = 2\pi r = \pi/4$, by the “average” velocity in the flow, which is

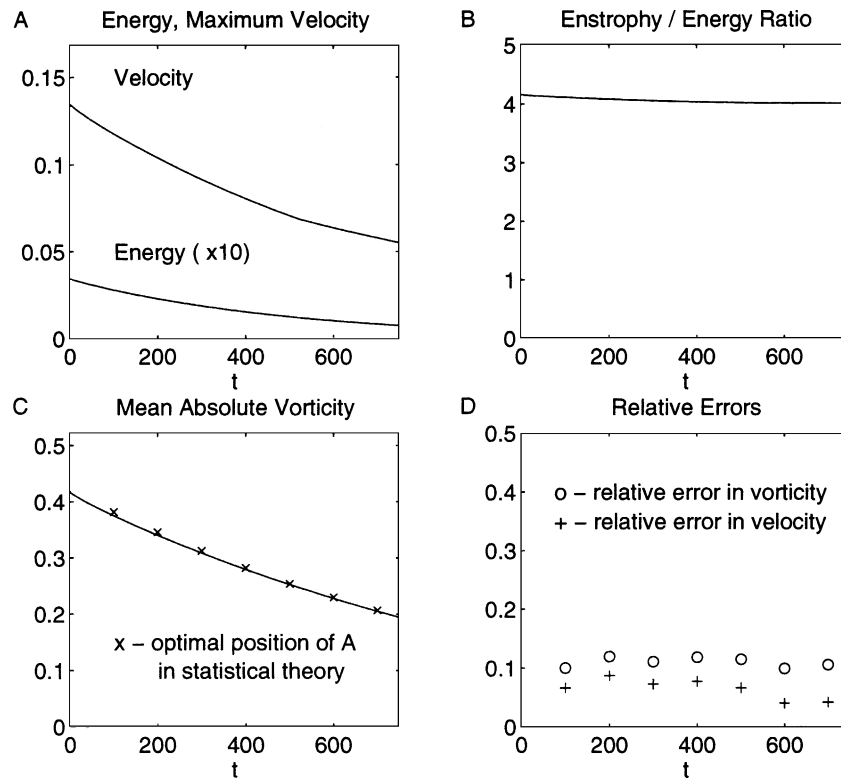


Fig. 6. Evolving quantities for the free decay of the vortex street shown in Fig. 3C, damped by a combination of Ekman drag, $d_0 = 10^{-3}$, and hyperviscosity, $d_3 = 10^{-7}$. (A) The energy and maximum velocity in the flow. (B) The enstrophy–energy ratio, which is normalized by π^2 . (C) The mean absolute vorticity in the flow and the optimal positions produced by the statistical theory. (D) The relative errors with respect to vorticity field, marked by \circ , and with respect to the velocity field, marked by \times .

approximately $v = 0.12/2$, so that

$$\text{Vortex turnaround time} = \frac{\pi}{4 \times 0.06} \sim 12. \quad (5.3)$$

Since the total run time for the numerical experiments in this section is $T = 750$, each run lasts more than 60 vortex turnaround times.

As the flow evolves, the individual vortices that comprise the initial street weaken and ultimately decay into a zonal shear flow. The energy, E , and absolute vorticity, \bar{A} , uniformly decrease, along with the maximum value of the velocity in the flow, which is shown in Fig. 6A and C. The circulation, Γ , is very close to zero throughout the run and is not shown. Initially, the circulation is zero, and the vortex street is symmetric with respect to the channel center.

A few snapshots of the evolving velocity field are provided in the left-hand column of Fig. 7, at times $t = 100$, 400, and 700. The weakening vortex street is seen in the upper two diagrams as the arrows indicating the direction and strength of the velocity field straighten and the pattern around the vortices becomes more elliptical. In the diagram shown in the bottom left-hand corner, the flow is a zonal shear and each of the arrows lies parallel to the channel boundaries. The predictions of the equilibrium theory, produced by the algorithm discussed in Section 4, are shown in right-hand column of Fig. 7. Each of the most-probable states has identical energy, and absolute

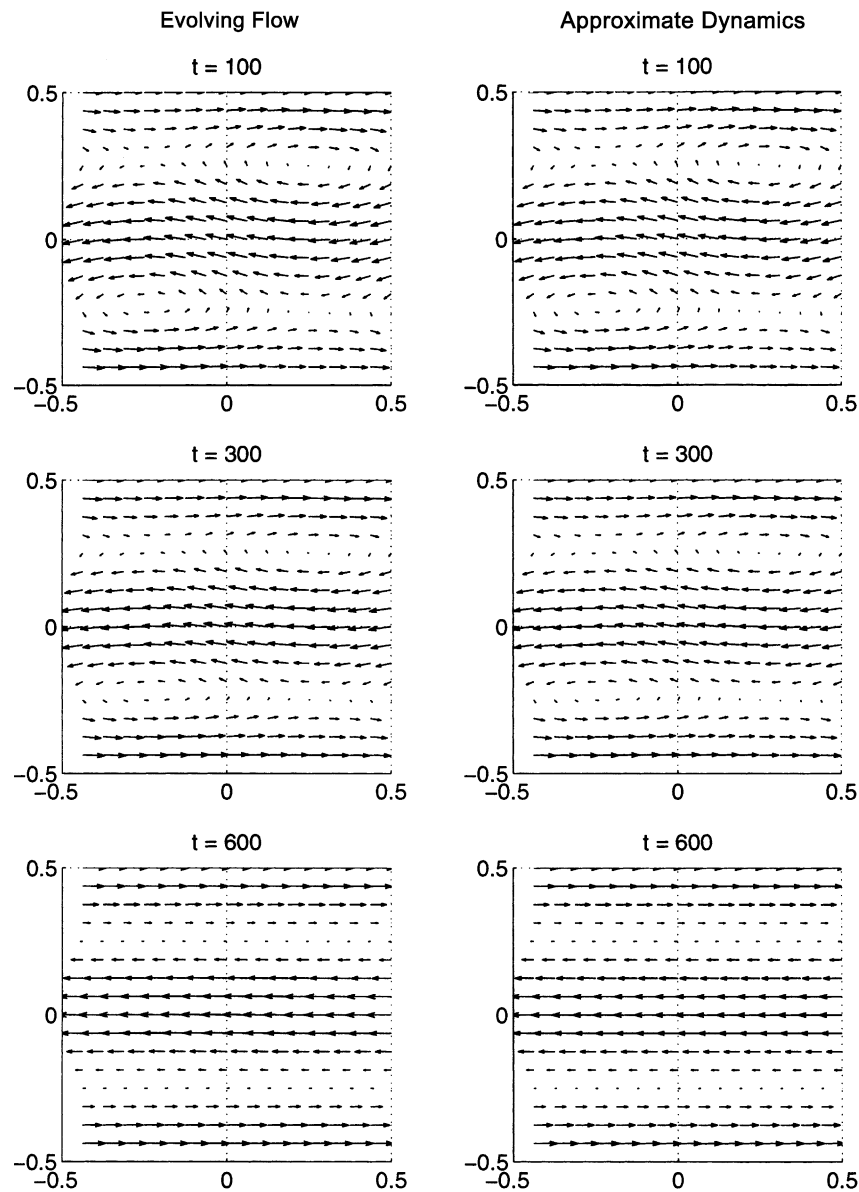


Fig. 7. Velocity field at times $t = 100, 300$ and 600 for the numerical experiment described in Fig. 6. Left-hand column: snapshots of the evolving flow; right-hand column: most-probable states of the statistical theory.

mean-field potential vorticity (the circulation very nearly vanishes) as the corresponding snapshot of the evolving flow. The matching velocity fields are indistinguishable by eye. The transition point from vortex to shear flow, which occurs near time $t = 520$, is also pinpointed by the approximate dynamics, although we do not provide a figure to show this.

The relative errors in the velocity and vorticity fields are shown in Fig. 6D. The magnitude of the errors between the evolving flow and the equilibrium solutions is very low; approximately 5–8% in the velocity fields and 10–12%

in the vorticity fields. We have also calculated the values of the mean-field absolute vorticity, \bar{A} , that produce most-probable states that are optimal, in the sense of correlations defined in (2.10); these values are plotted with \times 's in Fig. 6C. For these optimal fits, we match the energy and circulation of the evolving flow, but select the mean-field absolute vorticity that produces the lowest correlation with respect to the evolving flow. Notice that the positions of the optimal fit are quite close to the evolving mean-field absolute vorticity at all times, which gives strong support for the algorithm developed in Section 4. There is no practical difference between these “optimal” solutions and those produced by matching the energy, circulation and mean-field absolute vorticity in the evolving flow.

Finally, in Fig. 6B the evolution of the ratio of enstrophy to energy, Λ , in (2.14) shows that the freely decaying solution is approaching the ground state. The ratio is uniformly decaying to the limiting value of $4\pi^2$, as predicted by the selective-decay theorem described in Section 2.5.

6. Statistical consistency of damped and driven vortex states

In Section 5, we demonstrated the meta-stability of freely decaying monopole and dipole vortices initialized by most-probable states of an equilibrium statistical theory. Here, we provide more stringent tests on the approximate dynamics — in addition to damping by dissipation that includes both Ekman drag and hyperviscosity, the evolving flow is driven by small-scale vortices placed randomly in the channel, which mimics a forcing provided by small-scale storms in geophysical flow. We run a number of numerical experiments, including (1) the bombardment of monopole vortices with like-signed small-scale vortices, (2) the buildup of a large-scale shear flow via an inverse cascade driven by single-signed vortices, (3) the maintenance of vortex streets with dissipation and small-scale vortex forcing and (4) the emergence of vortex streets from an initial shear flow via an inverse cascade driven by small-scale vortices of both signs.

The key parameter in these experiments is the amplitude of the localized forcing, Amp. In the numerical runs initialized by a monopole vortex and forced with single-signed vortices, the quantitative fit between the evolving flow and the approximate dynamics generally improves and the small-scale forcing hastens the transition from vortex flow to shear flow. In the numerical runs initialized by a dipole vortex street and forced with vortices of both signs, the quantitative measures generally degrade with increased forcing strength. For a strong forcing with $\text{Amp} = \frac{3}{10}$ the peak initial potential vorticity in the flow, relative errors in the velocity measure are usually 20% and relative errors in the vorticity measure are usually 40%.

However, the small-scale forcing helps to maintain the vortex structure of the flow and the qualitative structure is usually captured by the equilibrium statistical theory; larger errors usually occur at higher forcing strengths. The degradation of the relative errors for stronger forcing is undoubtedly related to the dimples in the potential vorticity field due to small-scale vortices not yet strained by the large-scale flow. These corrugations in the potential vorticity surface naturally exert a greater effect on the relative error in the vorticity measure. A summary of the quantitative fit between the evolving flow and the approximate dynamics is provided in Table 1.

6.1. Forcing of vortex monopoles by small-scale, single-signed vortices

In this section, we add small-scale forcing with positive amplitude to the numerical runs initialized with the peaked monopole shown in Fig. 3A. The fluid is dissipated by a combination of Ekman drag, $d_0 = 10^{-3}$, and hyperviscosity, $d_3 = 10^{-7}$. The amplitude of the localized forcing vortices is fixed at $\text{Amp} = 0.1$, and is chosen so that the overall energy in the channel is roughly constant throughout the runs — energetically, the damping and driving are roughly in balance. The β -parameter is fixed at $\beta = 0.5$. In this example the quantitative fit provided by the equilibrium statistical theory improves in the presence of small-scale forcing when compared to the freely decaying monopole in Section 5.1, especially in the transition from vortex to shear flow.

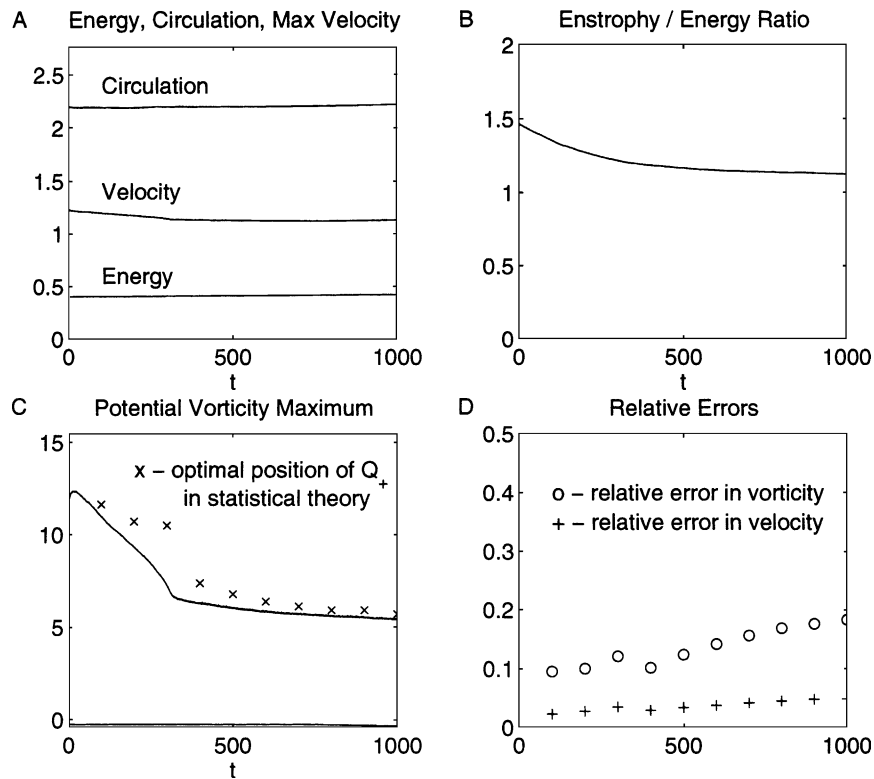


Fig. 8. As in Fig. 4, evolving quantities for the peaked monopole shown in Fig. 3A. Here, the flow is damped by a combination of Ekman drag, $d_0 = 10^{-3}$, and hyperviscosity, $d_3 = 10^{-7}$ and forced by small-scale vortices with $\text{Amp} = 0.1$.

The forcing and dissipation are roughly in balance and the energy, E , and circulation, Γ , change very little throughout the run, as shown in Fig. 8A and C. The vorticity maximum, however, drops rapidly from its peak near $Q_+ = 12$, following a small initial rise due to the influence of hyperviscosity. The transition from vortex street to shear flow is apparent from the kink in this curve that appears near the time $t = 400$. After this time the maximum vorticity in the shear flow continues to decline, but at a slower pace. Notice that the enstrophy–energy ratio Λ shown in Fig. 8B, falls uniformly throughout the run, decreasing towards $\Lambda = \pi^2$, as described in Section 2.5.

Compared to the freely decaying numerical experiment in Section 5.1, the small-scale forcing hastens the transition from monopole to shear flow, which occurs here near $t = 400$. In the left-hand column of Fig. 9, we show a series of snapshots of damped and driven flow at times $t = 100, 300$, and 500 . These images, which show the contour lines of the potential vorticity field, show that the weakening vortex at $t = 100$ and 300 has decayed into a shear flow by time $t = 500$. The equilibrium solutions of the approximate dynamics are shown in the corresponding positions of the right-hand column in Fig. 9. The qualitative structure of the decaying flow—whether vortex flow or zonal shear—is clearly captured by the approximate dynamics, which also pinpoints the time at which the evolving flow crosses from vortex to shear flow.

The relative errors in the velocity and vorticity fields are shown in Fig. 8D. The magnitude of the errors between the evolving flow and the equilibrium solutions is very low; approximately 3–5% in the velocity fields and 10–20% in the vorticity fields. As in Section 5.1, we calculate the optimal fit, in the sense of correlations, to the evolving flow. The optimal values of potential vorticity maxima are plotted with 'x's in Fig. 8C, which shows the evolving vorticity

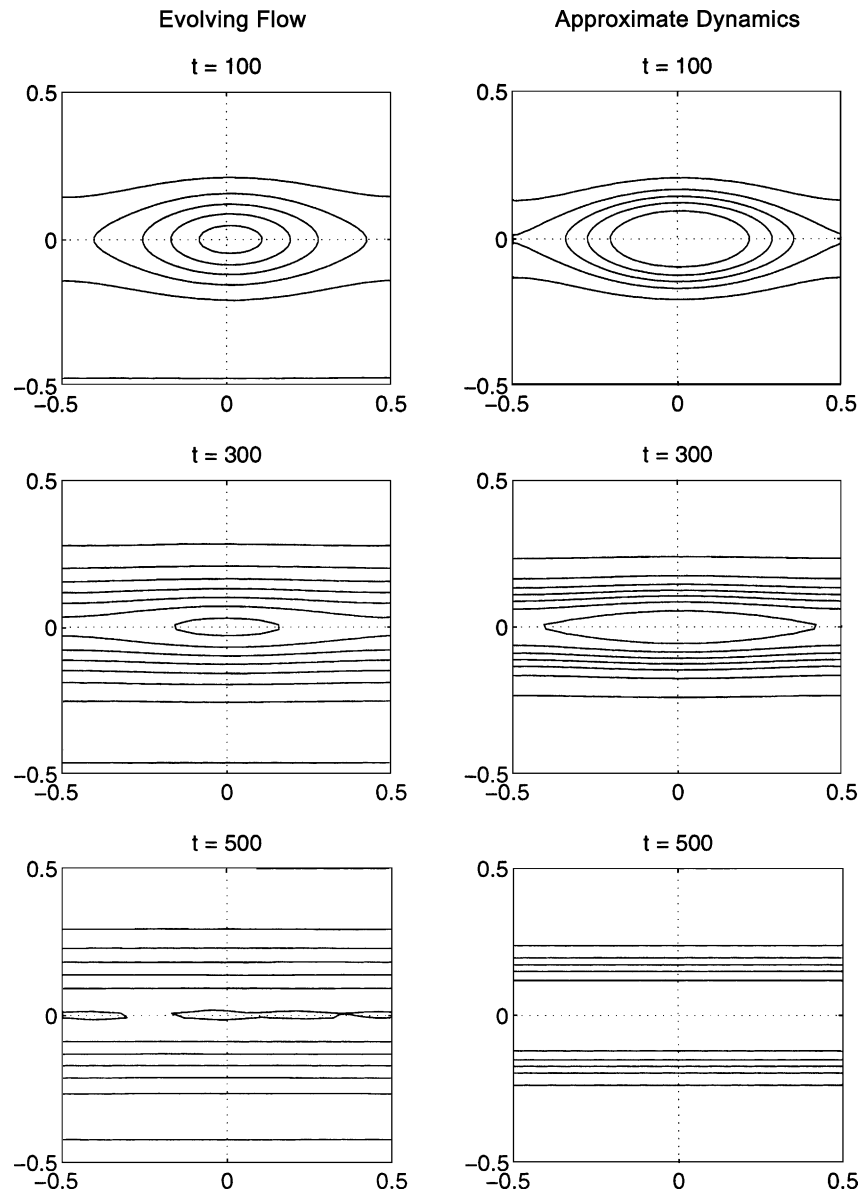


Fig. 9. Contour lines of the potential vorticity fields at times $t = 100, 300$ and 500 for the numerical experiment described in Fig. 8. Left-hand column: snapshots of the evolving flow; right-hand column: most-probable states of the statistical theory.

maxima in the flow. Notice that the position of the optimal fit is quite close to the evolving maxima at all positions except the times for the transition from vortex to shear flow, which occurs at $t = 400$. Here, the optimal value, $Q_+ \approx 10.5$, is somewhat higher than the maximum mean-field potential vorticity, $\bar{q}_{\max} \approx 6$. However, there is very little difference in the shape of these competing most-probable shear flow solutions — both are weak vortices at times earlier than the crossover point and shear flows at times afterwards. Moreover, the optimal fit yields a relative error in the velocity near 3%; the choice demanded by the algorithm, using (4.16), yields an error of 3.4%. Finally,

a comparison with the errors incurred by the freely decaying vortex depicted in Fig. 4D shows that the presence of small-scale forcing actually improves the performance of the approximate dynamics in the transition from vortex to shear flow.

6.2. Inverse cascade from small-scale forcing of single-signed vortices

A far more stringent test of the statistical theory is to build a large-scale structure by small-scale forcing of an initially quiescent flow. In order to encourage the formation of coherent structures, we eliminate the Ekman drag, which damps both large and small scales, from the dissipation, i.e., $d_0 = 0$ in the operator \mathcal{D} defined in (2.2), and damp the evolving flow solely with hyperviscosity, $d_3 = 10^{-10}$. The flow, computed here at 256×256 resolution, is forced by localized single-signed vortices with radius, $r = \frac{12}{256} (= \frac{3}{64})$, and amplitude, $\text{Amp} = 0.1$, placed at random locations in the channel at time intervals, $\Delta t = 0.1$. Thus, by the end of the numerical experiment at time $T = 1000$, we have bombarded the evolving flow with 10,000 localized vortices. Also, for simplicity in discussion we set $\beta = 0$ in these experiments. Although the emerging structures in these experiments are shear flows — accurately tracked by the approximate dynamics with errors in the velocity field approaching 3% after nearly 10,000 forcings — we have found some evidence that monopole vortices can arise as the most-probable state of the statistical theory provided that the dissipation is sufficiently weak and the forcing vortices are sufficiently small in scale.

The circulation, maximum velocity, and square root of the energy shown in Fig. 10A all grow linearly in this numerical run, which is a consequence of the relatively weak dissipation. The potential vorticity maxima, shown

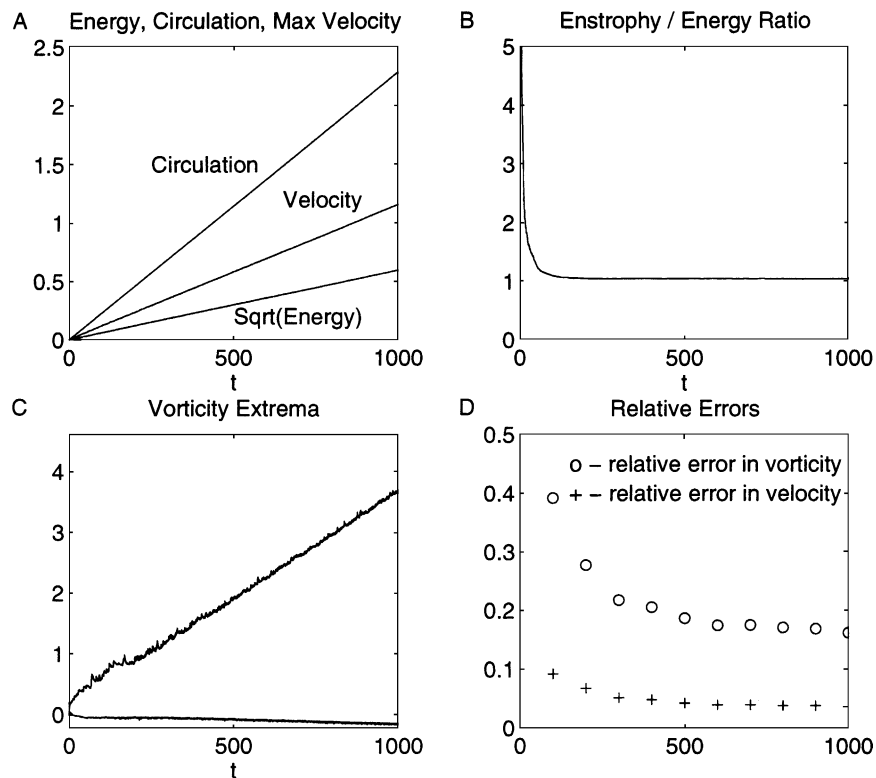


Fig. 10. As in Fig. 4, evolving quantities for initially quiescent flow in a channel. Here, the flow is only damped by hyperviscosity, $d_3 = 10^{-10}$, and forced by localized vortices with amplitude, $\text{Amp} = 0.1$.

in Fig. 10C, also grow linearly and exhibit a transition from a faster to slower rate of growth, which appears near time $t = 200$. The vorticity minima decrease slightly in the run due to the effects of hyperviscosity. In contrast to the smooth lines in Fig. 10A, the potential vorticity extrema depicted in Fig. 10C are jagged, showing the effects of random forcing.

In the left-hand column of Fig. 11, we show three snapshots of the potential vorticity surface of the evolving flow at times $t = 100, 500,$ and 1000 . The jaggedness of the surfaces clearly show the effects of the small-scale forcing. At time $t = 100$ individual vortices have begun to cluster, forming the zonal shear flow; by time $t = 1000$ the shear flow is strong, although it exhibits a curious rippling in the potential vorticity surface in the center of the channel. The most-probable states of the equilibrium theory are provided in the matching diagrams in the right-hand column of Fig. 11. Each of these solutions is formed from extracting the energy, E , circulation, Γ , and potential vorticity maximum, Q_+ , from the evolving snapshots, and solving the mean-field equation in (3.6) for these values.

Naturally, each of the steady most-probable solutions shown in the right-hand column of Fig. 11 are smooth, even for early times in the numerical run. We might reasonably expect that the quantitative fit between the evolving snapshots and the most-probable states of the equilibrium theory improves at longer times. This is shown in Fig. 10D, in which the relative errors in the vorticity field uniformly decrease from nearly 40% at time $t = 100$ to 16% at time $t = 1000$ and the relative errors in the velocity field uniformly decrease from 9 to 3% in the same time range. As in other experiments with small-scale forcing, the errors in the velocity field are much lower than the errors in the vorticity field. Indeed, the strongly forced evolving flow quickly nears the ground state, which is indicated in Fig. 10B by the rapid approach of enstrophy–energy ratio to its minimum value, $\Lambda = \pi$. A direct comparison of the most-probable states produced by the statistical theory to the linear ground state solutions, which are the eigenfunctions of the Laplacian operator for the channel domain as described in Section 2.5, shows that the two are closely correlated throughout the run, decreasing from a difference of 3% at time $t = 100$ to 2% at time $t = 1000$.

What is the effect of grid resolution on the numerical results discussed above? Fig. 12 depicts two snapshots of potential vorticity at $t = 100$, recomputed at the lower 64×64 and 128×128 grid resolutions. Up to this time, 1000 small vortices have been added to the evolving flow; yet it remains quite difficult to distinguish between the two potential vorticity fields. Moreover, bulk features of the flow are hardly affected by the change in resolution. For instance, the slopes of the square root of the energy, obtained from the two simulations at different resolutions, only vary by 0.5%.

The rippling in the potential vorticity surface in the instantaneous snapshots in Fig. 11 is a transitory phenomenon and disappears under sustained forcing at longer times. We show a similar rippling in the potential vorticity surface in Fig. 13 for a numerical run in which the dissipation by hyperviscosity is stronger, $d_3 = 10^{-7}$. Snapshots of the evolving flow are shown in the left-hand side of the figure at times $t = 100, 200,$ and 500 . Here, the potential vorticity surfaces at comparable times are much smoother than in Fig. 11, but still show a furrowing down the center of the channel at short times. By time $t = 500$, however, the evolving solution has flattened in the channel center. The most-probable states in the approximate dynamics, produced by matching the energy, circulation, and potential vorticity maximum in the evolving flow, are shown in the right-hand column of Fig. 13. At time $t = 500$, the relative errors are near 19% in the vorticity field and 4% and the velocity field. The relatively large errors in the vorticity field are due to the negative potential vorticity generated by the relatively strong hyperviscosity.

6.3. Maintenance of vortex streets by small-scale, double-signed forcing

In Section 5.2, we showed that freely decaying vortex streets are accurately tracked by the approximate dynamics; here we repeat these numerical experiments with the identical initial conditions and dissipation, adding small-scale forcing by localized vortices of both signs. In general, the forcing delays the transition from vortex to shear flow vortex streets, even as the vortices that make up the large-scale street are bombarded by localized vortices of the opposite sign.

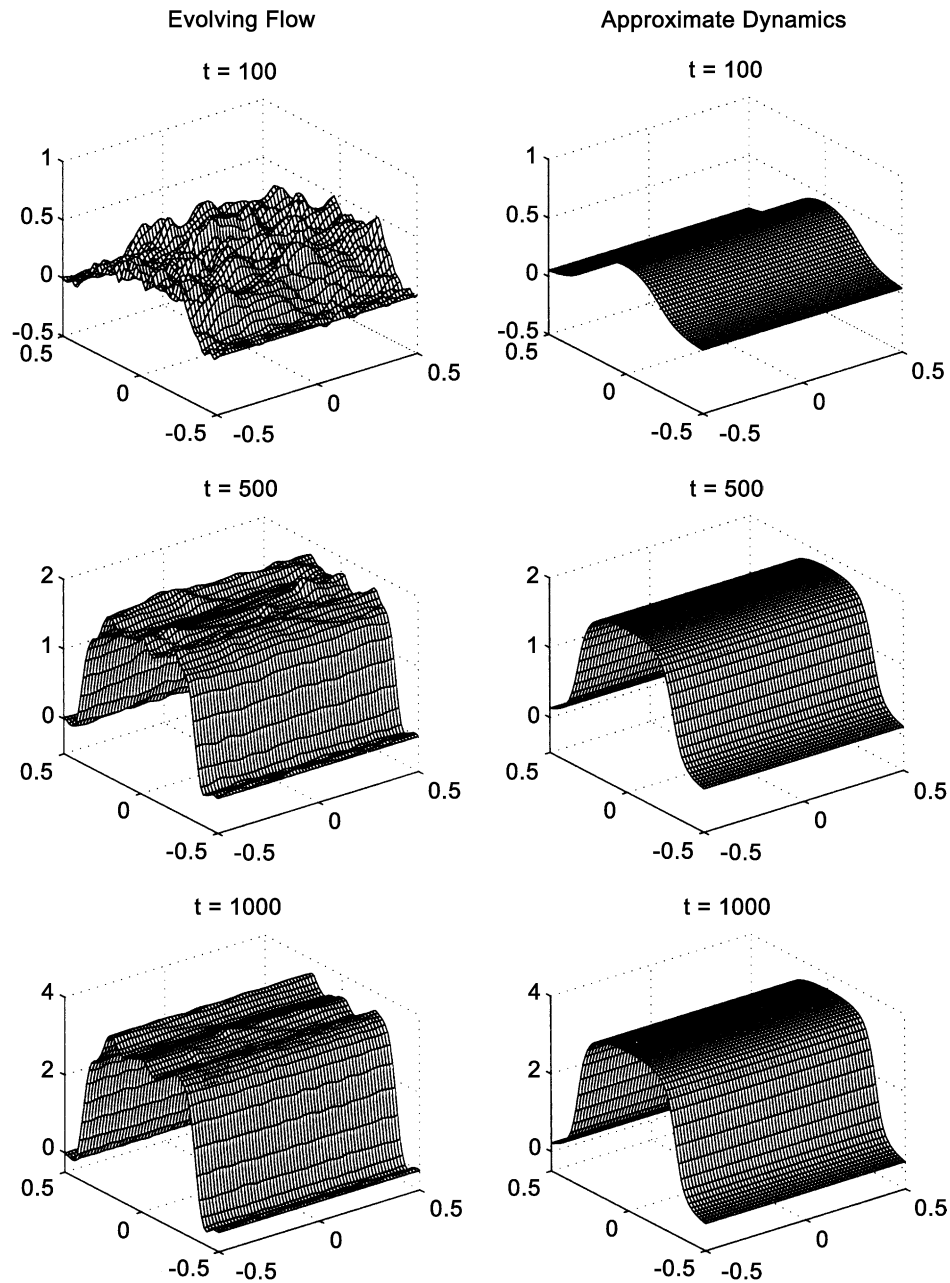


Fig. 11. Potential vorticity surfaces at times $t = 100, 500$ and 1000 for the numerical experiment described in Fig. 10. Left-hand column: snapshots of the evolving flow; right-hand column: most-probable states of the statistical theory.

We repeat the numerical experiment described in Section 5.2, retaining the level of dissipation and the geophysical β -parameter but adding small-scale vortices of amplitude, $\text{Amp} = 0.1$ and 0.3 , in two separate runs. As in Section 6.1 the small-scale forcings are placed at random grid points on the channel at regular intervals, $\Delta t = 0.1$, and each such vortex has identical radius, $r = 3$ grid points, where the full channel width is 64 grid points.

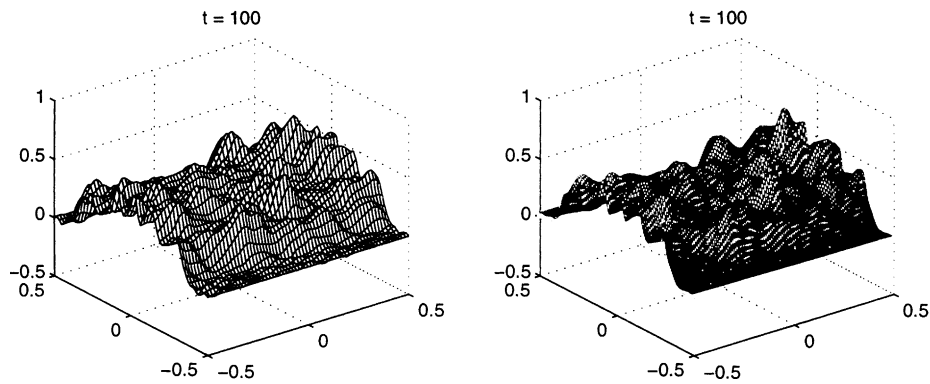


Fig. 12. Potential vorticity surface at times $t = 100$ for the numerical experiment described in Fig. 10. Left: computed at 64×64 resolution; right: computed at 128×128 resolution.

For the weaker case with $\text{Amp} = 0.1$, the topological transition from vortex street to shear flow is delayed by the small-scale forcing, which helps to maintain the vortical structure in the flow. Indeed, the evolving flow never quite reverts to a zonal shear, but retains a slight signature of the dipolar pattern in the velocity field. The approximate dynamics tends to slightly underpredict the strength of the vortex street, predicting shear flows where the evolving flow contains weak vortex street. Quantitatively, the approximate dynamics performs quite well in this case, with relative errors in the velocity field between 8 and 20% and relative errors in the vorticity field between 15 and 35% throughout the run.

For the stronger case with $\text{Amp} = 0.3$, a strong vortex street is maintained throughout the run. The strength of the forcing can be seen in the jaggedness of the key quantities in the flow shown in Fig. 14, including energy, E , and mean-field absolute vorticity, \bar{A} . The enstrophy–energy ratio, which is depicted in Fig. 14B, holds roughly constant throughout the initial stages of the run, and increases towards the end, which suggests that energy introduced by the localized forcing is entering into the smaller scales. As the largest scales continue to decay—the energy is decreasing throughout the run—the forcing, whose amplitude is held fixed, becomes relatively stronger, and helps to maintain the vortex street.

A few snapshots of the evolving velocity field are provided in the left-hand column of Fig. 15 at times $t = 100$, 400, and 700. The vortex street remains quite strong throughout the run, with well-formed vortices and a clear meander to the jet that traverses the center of the channel. The predictions of the equilibrium theory are shown in right-hand column of Fig. 15. Each of these most-probable states has identical energy, circulation, and absolute mean-field potential vorticity as the corresponding snapshot of the evolving flow.

The quantitative diagnostics for the experiment, the correlation and relative errors in the velocity and vorticity fields, are shown in Fig. 14D. The errors in both the velocity and vorticity fields have increased at the higher forcing amplitude: the errors in the velocity field are approximately 20%, excluding the time period between $t = 500$ and 600, where the approximate dynamics fails, and the errors in the vorticity field are approximately 40%. For the interval of time between $t = 500$ and 600 the relative velocity errors in the approximate dynamics reach 50%. In this narrow interval of time the equilibrium statistical theory incorrectly produces a shear flow as the most-probable state based on the evolving energy, circulation, and absolute vorticity. The rapid increase in the relative errors in the velocity and vorticity fields shows the importance of predicting the correct topological structure in the evolving flow.

Although the relative errors in the velocity field have increased to nearly 20% in this run, the approximate dynamics clearly captures the qualitative structure of the velocity field in the evolving flow as is demonstrated in Fig. 15. The relative errors in the potential vorticity field have increased to nearly 40%; however, the basic structure of the vortex

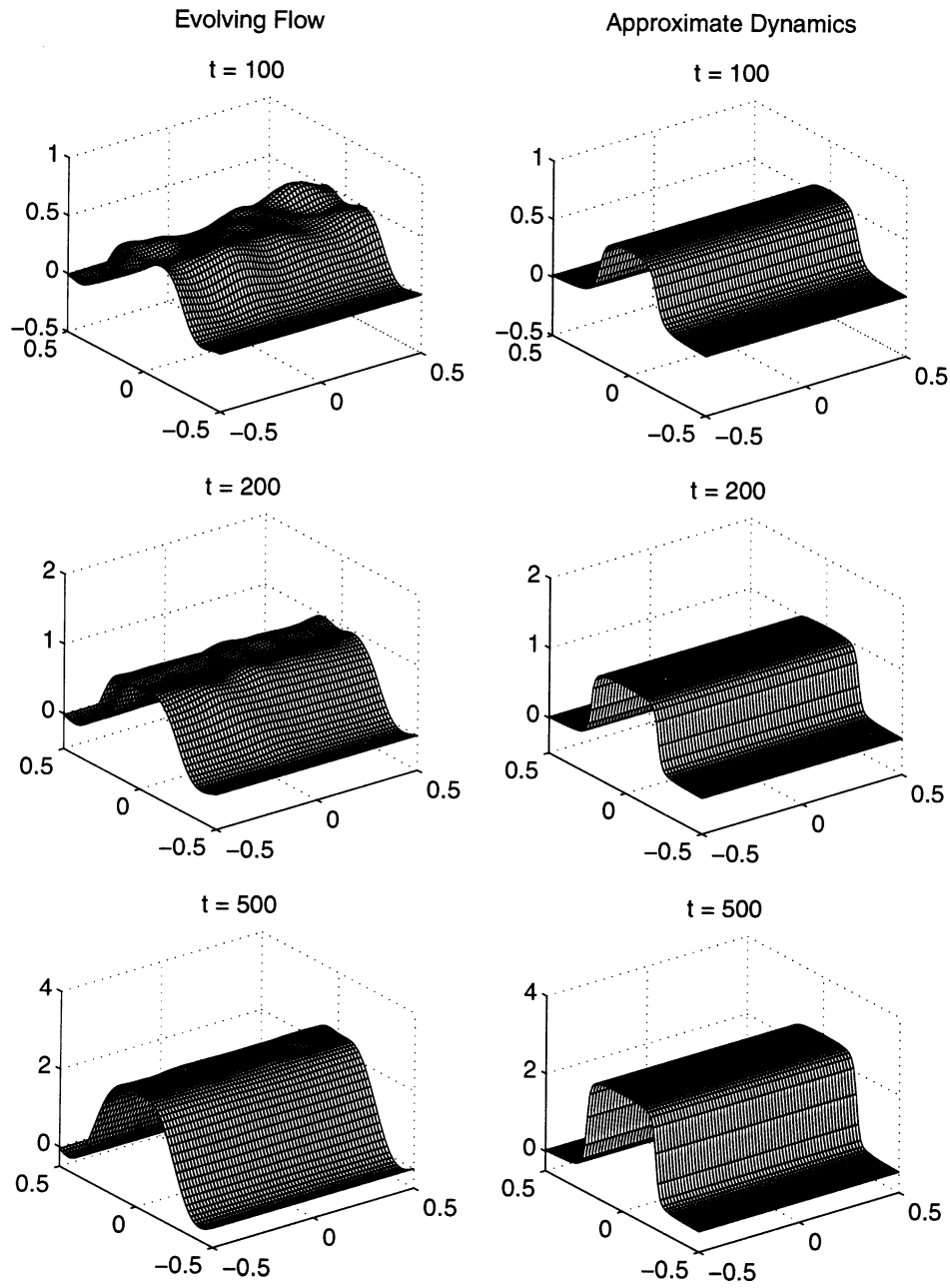


Fig. 13. Potential vorticity surfaces at times $t = 100, 200$ and 500 for initially quiescent flow in a channel, damped by hyperviscosity, $d_3 = 10^{-7}$, and forced by localized vortices with amplitude, $\text{Amp} = 0.1$. Left-hand column: snapshots of the evolving flow; right-hand column: most-probable states of the statistical theory.

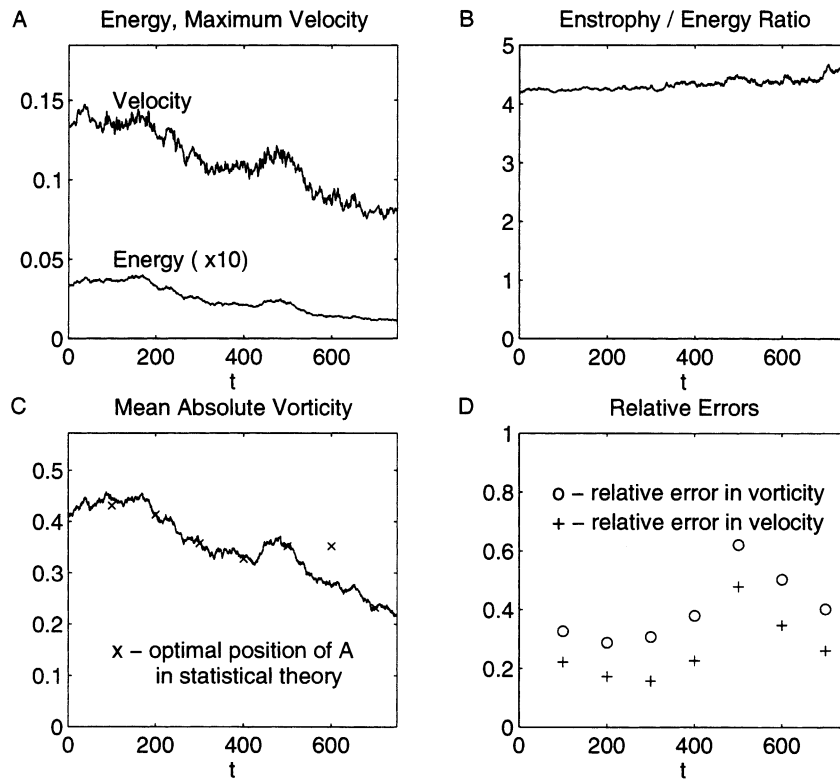


Fig. 14. As in Fig. 4, evolving quantities for the vortex street shown in Fig. 3C undergoing damping and driving. The flow is damped by a combination of Ekman drag, $d_0 = 10^{-3}$, and hyperviscosity, $d_3 = 10^{-7}$, and strongly forced by small-scale vortices with amplitude, $|\text{Amp}| = 0.3$.

street is also seen in the potential vorticity surfaces produced by the approximate dynamics. In the left-hand column of Fig. 16, we provide the evolving PV surfaces at times $t = 100, 400$ and 700 . Here, the strong small-scale forcing, which includes localized vortices of both signs, introduces large ripples into the potential vorticity surfaces of the evolving flow. The most-probable states of the equilibrium theory are shown in the right-hand column of Fig. 16. The equilibrium most-probable states are much smoother than the evolving flow field; nevertheless, the strong cores of the damped and driven vortex streets are clearly reproduced. The degradation of the relative errors in the vorticity field is predominantly caused by the large dimples in the PV field due to localized vortices that have not yet been strained by the large-scale street. A comparison between the velocity fields in Fig. 15, which are largely smooth even in the evolving snapshots, and the potential vorticity fields in Fig. 16, demonstrate that the error in the relative vorticity is a much tougher measure for the approximate dynamics.

Again, comparison of two numerical solutions, computed at 64×64 and 128×128 resolution, shows that the resolution used is sufficient. At $t = 100$, the instantaneous difference in potential vorticity fields computed at the two resolutions does not exceed 7% — note that 1000 small vortices have been added. Moreover, the maximal relative error in energy over the entire time interval up to $T = 750$ remains below 4%.

6.4. Vortex coalescence in strongly forced shear flow

In Section 6.3, we showed that the approximate dynamics performs reasonably well in tracking the evolution of vortex streets bombarded by localized vortices, even at forcing amplitudes at nearly $\frac{3}{10}$ the peak vorticity in

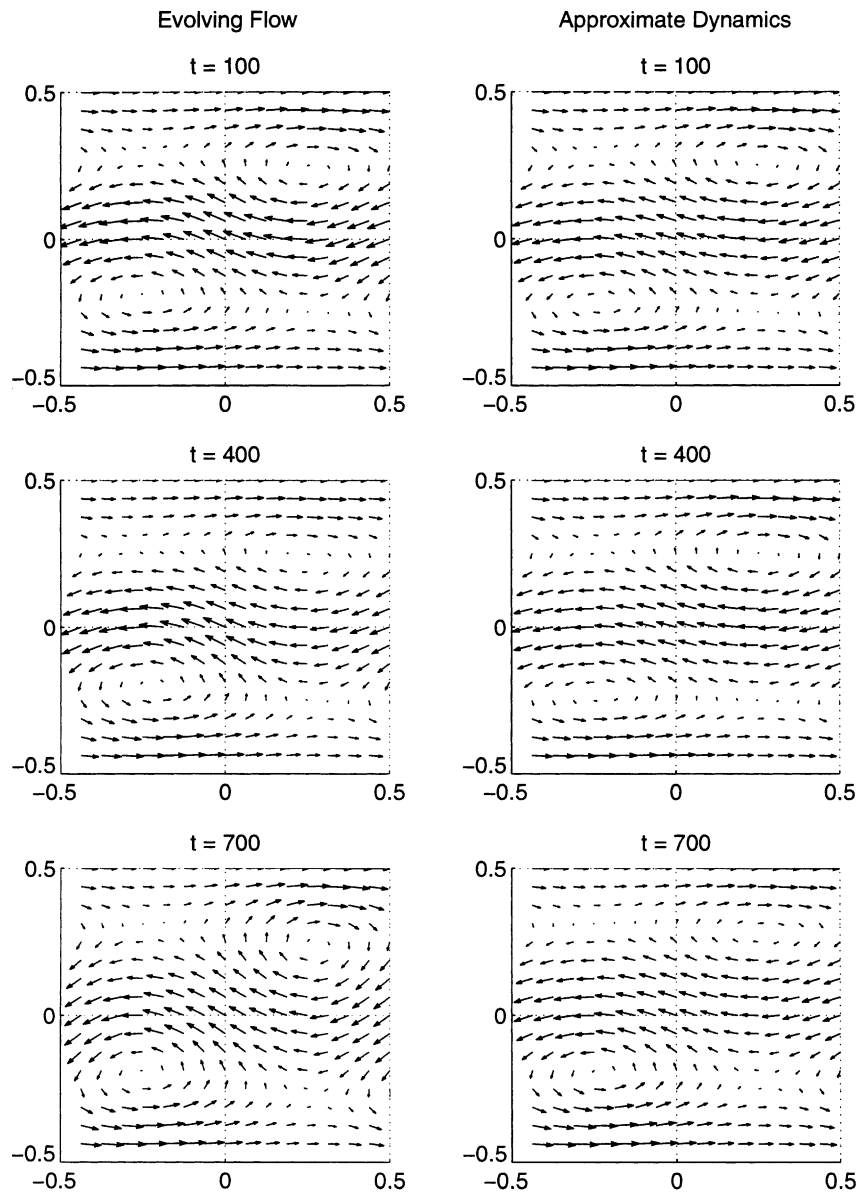


Fig. 15. Velocity field at times $t = 100, 400$ and 700 for the numerical experiment described in Fig. 14. Left-hand column: snapshots of the evolving flow; right-hand column: most-probable states of the statistical theory.

the initial flow. Here, we test the statistical theory under far more stringent conditions: we repeat the damped and driven numerical experiments run in Section 6.3 — damped by a combination of Ekman drag and hyperviscosity and driven by small-scale vortices of both signs with the large amplitude, $|\text{Amp}| = 0.3$ — and replace the initial vortex street with the initial shear flow shown in Fig. 3D. During the numerical run the localized forcing eventually creates and maintains a vortex street in the channel.

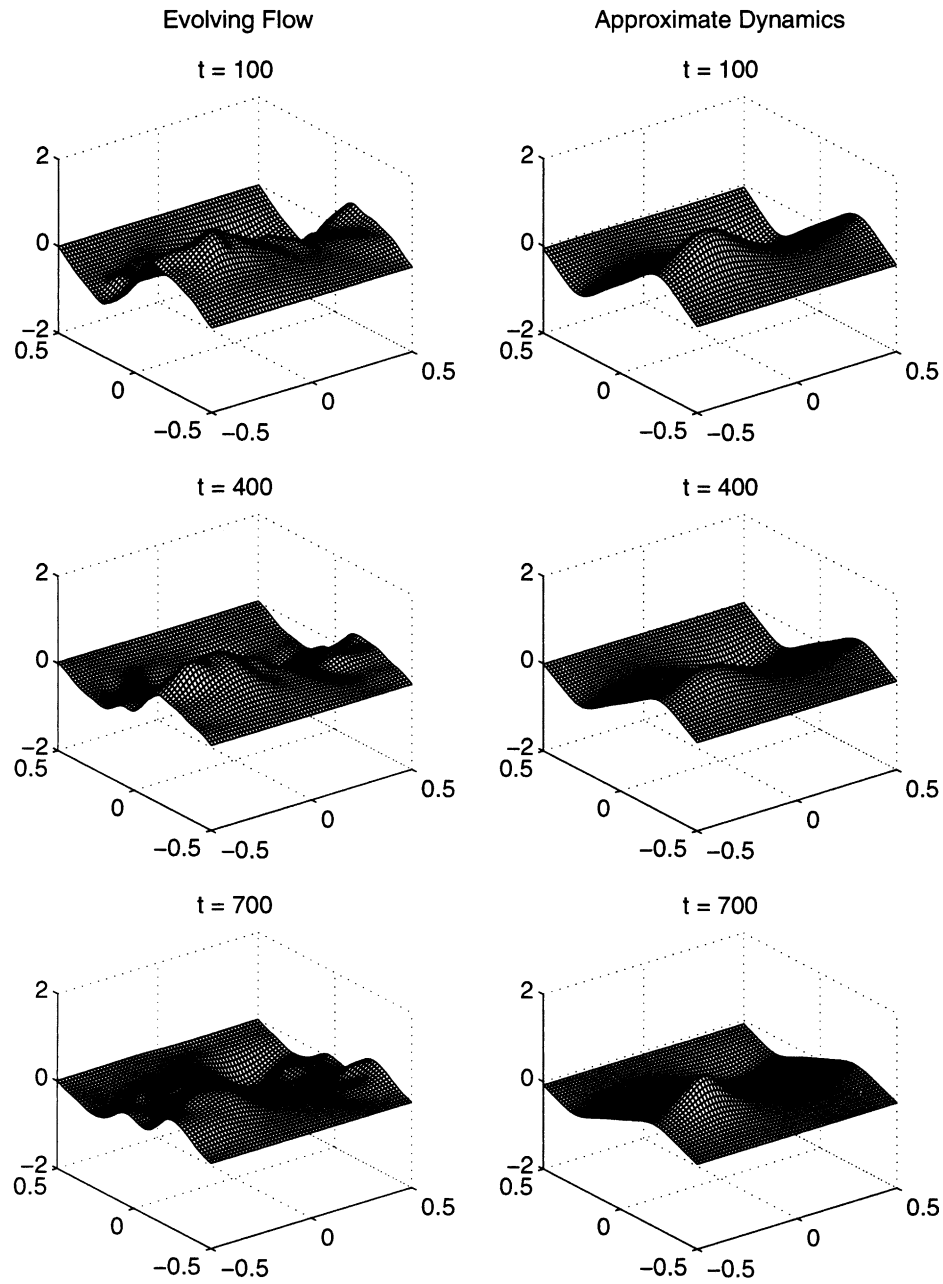


Fig. 16. Potential vorticity field at times $t = 100, 400$ and 700 for the numerical experiment described in Fig. 14. Left-hand column: snapshots of the evolving flow; right-hand column: most-probable states of the statistical theory.

The evolution of key quantities in the flow, which includes the energy, absolute vorticity and maximum velocity, are shown in Fig. 17A and C. The energy, absolute vorticity and maximum velocity generally decrease during the length of the numerical experiment. The jaggedness in these curves is caused by the localized vortices added to the potential vorticity field.

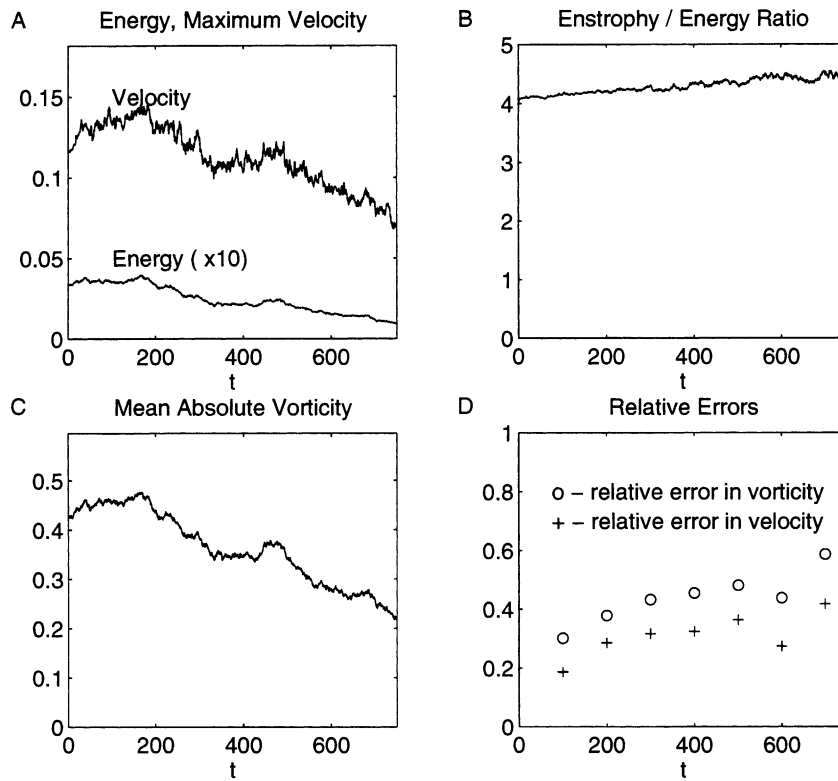


Fig. 17. As in Fig. 4, evolving quantities for an initial shear flow shown in Fig. 3D undergoing damping and driving. The flow is damped by a combination of Ekman drag, $d_0 = 10^{-3}$, and hyperviscosity, $d_3 = 10^{-7}$, and strongly forced by small-scale vortices with amplitude, $|\text{Amp}| = 0.3$.

The main effect of the small-scale forcing is to induce and maintain a vortex street in the evolving flow. Although the initial flow field is a zonal shear, the small-scale forcings quickly coalesce into the counter-rotating vortices characteristic of the street. A few snapshots of the evolving velocity field are provided in the left-hand column of Fig. 18 at times $t = 100, 300$, and 640 . A weak vortex street is seen in the upper diagram; it gradually strengthens as time evolves, as is evident in the lower diagrams in the column.

The predictions of the equilibrium theory, which are calculated by the approximate dynamics described in Section 4, are shown in the right-hand column of Fig. 18. Each of these most-probable states has identical energy, circulation, and absolute mean-field potential vorticity as the corresponding snapshot of the evolving flow. Here, the approximate dynamics tends to predict shear flows—see times $t = 100$ and 300 —for the weaker vortex streets in the evolving flow. At time $t = 640$, where the strength of the evolving street has strengthened as indicated by the increasing meander in the central jet, the equilibrium theory produces a vortex street, although weaker than the evolving flow. Throughout the run the approximate dynamics tends to qualitatively underpredict in this fashion, producing zonal shears for weak streets and weak vortex streets for strong ones.

Quantitatively, the relative errors, which are shown in Fig. 17D, are fairly high, usually between 20 and 40% in the velocity field and between 30 and 60% in the vorticity field. This is not unexpected given the stringency of the test—tracking a vortex flow induced by small-scale forcing in an initial shear flow. For the times when the

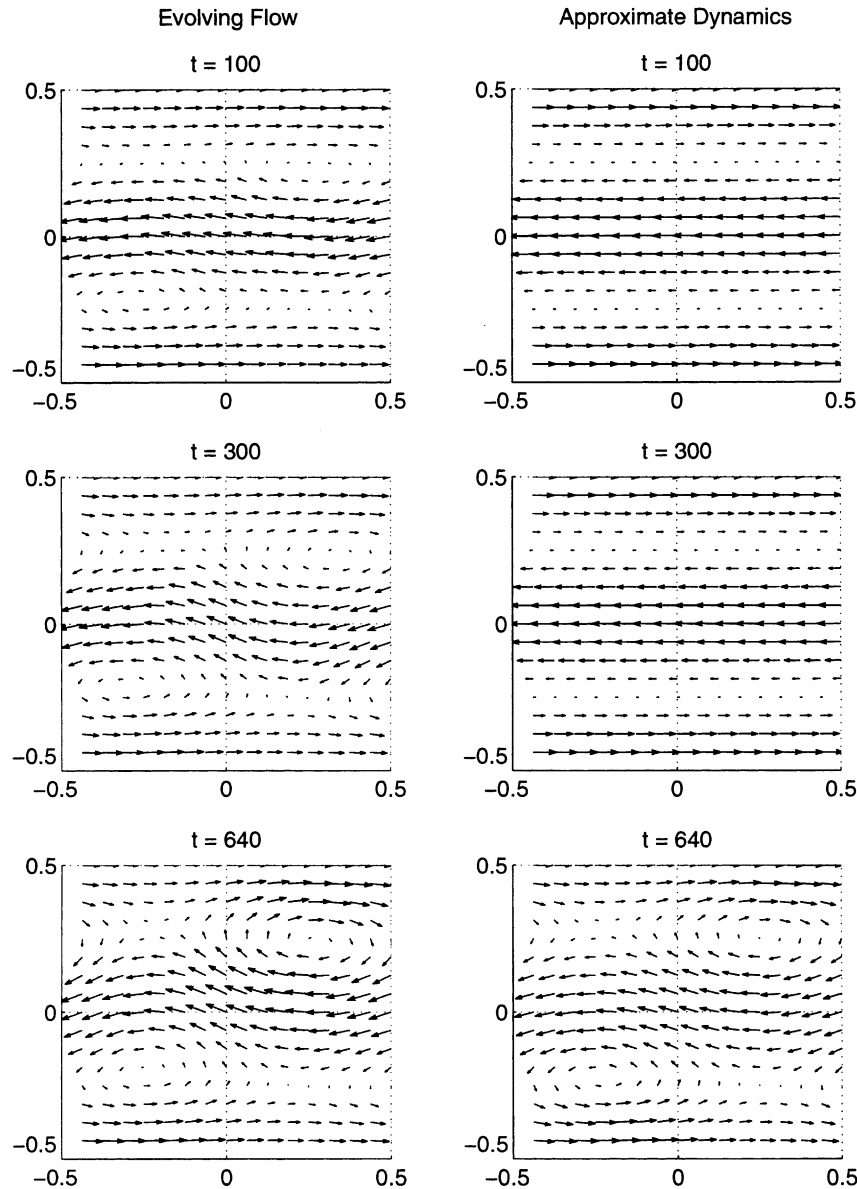


Fig. 18. Velocity field at times $t = 100, 300$ and 640 for the numerical experiment described in Fig. 17. Left-hand column: snapshots of the evolving flow; right-hand column: most-probable states of the statistical theory.

most-probable state achieves the correct topological structure, the relative errors, especially in the velocity field, are in the lower portions of these ranges. Indeed, for the strong vortex street that appears at time, $t = 640$, which is shown in the bottom row of Fig. 18, the errors in the velocity field fall to 16%. Thus, the approximate dynamics is capable of tracking the transition from zonal shear to vortex flow induced by small-scale forcing, although it tends to underpredict the strength of the vortex street and frequently predicts zonal shears if the vortex street is sufficiently weak.

7. Conclusion

In this paper, we have demonstrated the meta-stability in both direct and inverse cascades of the most-probable states of an equilibrium statistical theory — including monopole vortices and dipole vortex streets — in evolving, damped and driven QG flow in a periodic β -plane channel. Numerical experiments have included vortex structures undergoing (1) pure decay by a combination of Ekman drag and hyperviscosity in Section 5, and (2) bombardment by small-scale vortices placed at random positions in the channel in Section 6. In all runs the state of the evolving flow remains close to the predictions of the equilibrium theory, even as the energy substantially decreases and the fluid follows topological transitions from vortex to shear flow, and vice versa. Thus, the most-probable states of equilibrium statistical theory are useful models for the large-scale coherent structures that appear in atmospheric and oceanographic flows.

In Section 4, we introduced an algorithm that computes most-probable states from snapshots of the evolving QG flow. This “approximate dynamics” is based on just a few essential quantities in the evolving fluid — the energy, circulation, and potential vorticity extrema in (3.5) — for flows in which the vorticity is predominantly either positive or negative — or the energy, circulation, and absolute vorticity in (3.8) — for flows in which the vorticity is double-signed. The accuracy of the approximate dynamics is quantitatively measured by calculating the relative errors of the velocity and vorticity fields in (2.12) and (2.13) of the predictions from the equilibrium theory with respect to the snapshots of the evolving flow field. In all but the most rigorous of the numerical experiments, the quantitative fit is quite good, with low relative errors — especially in the velocity field — that vary with the strength of the forcing, the type of dissipation, and the initial coherent structure.

For the evolving monopoles the approximate dynamics performs equally well in the experiments undergoing free decay in Section 5.1 and those with both damping and driving in Section 6.1. Errors in the velocity field are typically around 5% and errors in the vorticity field are typically between 10 and 20%. The action of small-scale forcing, whose magnitude was chosen to roughly balance the dissipation, appears to hasten the decay of vortex to shear flow. In all of the monopole experiments the transition from vortex to shear flow is nearly pinpointed by the approximate dynamics. Also, in a series of inverse cascade experiments described in Section 6.3, we showed that the small-scale forcing establishes a large-scale zonal shear that is accurately predicted by the approximate dynamics, usually within 3% error in the velocity field at moderate times in the evolution.

We also show in Section 5.1 a subtle effect of hyperviscosity on the predictions by the equilibrium theory for monopole vortices. Vorticity maxima are not preserved under dissipation with hyperviscosity, and the numerical evolution of initially patch-like vortices leads to a sharp build-up of potential vorticity in the monopole center. Since the conservation of vorticity extrema is a key assumption in the Langevin statistical theory, which is discussed in Section 3, it is unsurprising that the approximate dynamics meets with somewhat less success in this case.

For the evolving dipole vortex streets in Sections 5.2 and 6.3 the accuracy of the approximate dynamics is dependent on the strength of the localized forcing. The decrease in accuracy is natural, however, as the localized forcing dimples the surface of the potential vorticity field. With free decay, i.e. no forcing, the approximate dynamics is most accurate, with relative errors in the velocity field near 5% and relative errors in the vorticity field near 12%. The flow also approaches the ground state predicted by the selective-decay theorem.

For weak forcing, where the amplitude of the small-scale localized vortices is approximately $\frac{1}{10}$ the magnitude of the maximum vorticity of the initial street, the approximate dynamics yields relative errors in the velocity field near 10% and relative errors in the vorticity field near 20%. The small-scale forcing maintains weak vortex streets that are very close to shear flows, which are predicted by the equilibrium theory.

For strong forcing, where the amplitude of the small-scale localized vortices is approximately $\frac{3}{10}$ the magnitude of the maximum vorticity of the initial street, the approximate dynamics yields relative errors in the velocity field near 20% and relative errors in the vorticity field near 40%. Here, the small-scale forcing excites strong vortex

streets that are maintained throughout the run. Excepting for a narrow interval of time in which the equilibrium theory predicts a zonal shear, a strong vortex pair is also produced by the approximate dynamics. For the even more rigorous test of strong forcing of an initial zonal shear flow described in Section 6.4 the approximate dynamics captures the overall tendency of the vortex street induced by the small-scale forcing, however, it tends to predict shear flows for weak vortex streets in the flow and underpredict the strength of the strong vortex streets that appear in the evolving flow.

Thus, for a wide range of numerical experiments the quantitative fit for the approximate dynamics is quite good for both monopole vortices and dipole vortex streets, which model large-scale geophysical structures, that evolve under damping and driving. The accuracy of the statistical predictions depends on the strength of the dissipation and forcing, best for the cases of pure decay and single-signed forcing, less successful for more stringent tests with strong forcing of both signs. Qualitatively, the approximate dynamics accurately tracks the topological structure of the evolving flow — whether vortex or zonal shear flow — and even tracks topological transitions in the numerical run from vortex flow to zonal shear, and vice versa.

Acknowledgements

Many of the numerical experiments described in this paper were performed on the Cray T90 at the San Diego Supercomputer Center. M. DiBattista is supported as a post-doctoral fellow at the Courant Institute by grants NSF DMS-9625795 and ONR N00014-96-0043. The research of A. Majda is partially supported by grants ONR N00014-96-0043, NSF DMS-9625795, and ARO DAAG55-98-1-0129.

References

- [1] F.B. Bretherton, D.B. Haidvogel, Two-dimensional turbulence above topography, *J. Fluid Mech.* 78 (1976) 129–154.
- [2] G. Carnavale, J. Frederiksen, Nonlinear stability and statistical mechanics of flow over topography, *J. Fluid Mech.* 175 (1987) 157–181.
- [3] M.T. DiBattista, A.J. Majda, An equilibrium statistical theory for large-scale features of open-ocean convection, *J. Phys. Oceanogr.* 30 (2000) 1325–1353.
- [4] M.T. DiBattista, A.J. Majda, B. Turkington, Prototype geophysical vortex structures via large-scale statistical theory, *Geophys. Astrophys. Fluid Dyn.* 89 (1998) 235–283.
- [5] W. E, C.-W. Shu, Effective equations and the inverse cascade theory for Kolmogorov flows, *Phys. Fluids A* 5 (1993) 998–1010.
- [6] G.R. Flierl, Isolated eddy models in geophysics, *Annu. Rev. Fluid Mech.* 19 (1987) 493–530.
- [7] C. Foias, J.L. Saut, Asymptotic behavior as $t \rightarrow \infty$ of solutions of Navier–Stokes equations and nonlinear spectral manifolds, *Indiana Univ. Math. J.* 33 (1984) 459–477.
- [8] M.J. Grote, A.J. Majda, Crude closure dynamics through large-scale statistical theories, *Phys. Fluids* 9 (1997) 3431–3442.
- [9] M.J. Grote, A.J. Majda, Crude closure for flow with topography through large-scale statistical theory, *Nonlinearity* 13 (2000) 569–600.
- [10] G. Holloway, Eddies, waves, circulation and mixing: statistical geofluid mechanics, *Annu. Rev. Fluid Mech.* 18 (1986) 91–147.
- [11] R.H. Kraichnan, Statistical dynamics of two-dimensional flow, *J. Fluid Mech.* 67 (1975) 155–175.
- [12] S. Legg, J. Marshall, A heton model of the spreading phase of open-ocean deep convection, *J. Phys. Oceanogr.* 23 (1993) 1040–1056.
- [13] A.J. Majda, M. Holen, Dissipation, topography, and statistical theories for large-scale coherent structure, *Commun. Pure Appl. Math.* 50 (1997) 1183–1234.
- [14] P.S. Marcus, Jupiter’s Great Red Spot and other vortices, *Annu. Rev. Astrophys.* 31 (1993) 523–573.
- [15] J. Miller, P.B. Weichman, M.C. Cross, Statistical mechanics, Euler’s equation, and Jupiter’s Red Spot, *Phys. Rev. A* 45 (1992) 2328–2359.
- [16] J. Pedlosky, *Geophysical Fluid Dynamics*, Springer, Berlin, 1979.
- [17] P. Rhines, Waves and turbulence on a β -plane, *J. Fluid Mech.* 69 (1975) 417–443.
- [18] R. Robert, A maximum entropy principle for two-dimensional Euler equations, *J. Statist. Phys.* 65 (1991) 531–553.
- [19] R. Salmon, G. Holloway, M.C. Henderschott, The equilibrium statistical mechanics of simple quasi-geostrophic models, *J. Fluid Mech.* 75 (1976) 691–703.
- [20] S.-Y. Shim, Ph.D. Thesis under A.J. Majda, New York University, New York, 1999.
- [21] B. Turkington, Statistical equilibrium measures and coherent states in two-dimensional turbulence, *Commun. Pure Appl. Math.* 52 (1999) 781–809.
- [22] B. Turkington, N. Whitaker, Statistical equilibrium computations of coherent structures in turbulent shear layers, *SIAM J. Sci. Comput.* 17 (1996) 1414–1433.